Supporting Information:

Spectroscopic and computational study of the interaction of Pt(II) pyrrole-imine chelates with human serum albumin

Sheldon Sookai[a] and Orde Q. Munro[a,b]*

[a] *Molecular Sciences Institute, School of Chemistry, University of the Witwatersrand, PO WITS 2050, Johannesburg, South Africa*

E-mail: s.sookai92@gmail.com

[b] *School of Chemistry, University of Leeds, Woodhouse Lane, LS2 9JT, UK*

E-mail: o.munro@leeds.ac.uk

1. Contents

---

2. General experimental methods

Pyrrole-2-carboxaldehyde, 1,3-diaminopropane, 1,3-diaminopropan-2-ol, 1,3-diamino-2,2-dimethyl propane, (R)-(+)-1,2-diaminopropane·2HCl and (S)-(-)-1,2-diaminopropane·2HCl were all purchased from Sigma-Aldrich. All organic solvents were of HPLC grade and were used without any further purification (DMSO, DMF, THF, ethyl acetate, methanol, DCM, and hexane). Buffer reagents included potassium hydroxide (≥ 90%) flakes and potassium monobasic phosphate buffer (KH_2PO_4 ≥ 99 ACS); these were purchased from Sigma Aldrich along with lyophilized fatty acid-free HSA (≥ 97%).

3. Instruments

3.1.1. Crystallography

Single crystal X-ray data sets were recorded with a four-circle Bruker D8 Venture X-ray diffractometer equipped with a Photon II CPAD area detector and a three-circle Bruker Apex II X-ray diffractometer employing a CCD area detector; both instruments were fitted with a fine-focus sealed X-ray tube source (Mo anode). Crystals were mounted under Paratone® oil on nylon loops (Hampton Research) and the crystals were kept at 173(1) K during data collection (Oxford CryoStream 700). Using Olex2,[1] the structure of **2** was solved with the ShelXT[2] structure solution program (intrinsic phasing) and refined with ShelXL[3] using least squares minimization. Olex2.solve-1.5 and Olex2.refine-1.5 were used to solve and refine the structure of **1**.

During refinement of the X-ray structure of **1**, it became apparent that disordered solvent was present in the lattice. A solvent mask was calculated, and 98 electrons were found in a volume of 172 $Å^3$ in 1 void per unit cell. This is consistent with the presence of 4.50 H_2O molecules per asymmetric unit which account for 90 electrons per unit cell. The final X-ray structure model was then refined to completion employing this solvent mask. From the SHELXL refinement, the highest difference peak was 1.902 *e* $Å^{-3}$ located at the coordinates [x, y, z] = [0.5145, 0.6322, 0.4701], precisely 0.723 Å from Pt1C and roughly in the same plane as the Pt(II) ion within the chelate ring. This same residual electron density peak was flagged with a C-level alert in the IUCr *checkCIF* algorithm (2.19 *e* $Å^{-3}$, 0.75 Å from Pt1C).

During refinement of the X-ray structure of **2**, it became apparent that disordered solvent was present in the lattice. A solvent mask was calculated, and 27 electrons were found in a volume of 229 $Å^3$ in 3 voids per unit cell. This is consistent with the presence of 1.20 H_2O molecules per asymmetric unit which account for 25 electrons per unit cell. The final X-ray structure model was then refined to completion employing this solvent mask. The highest difference peak (0.961

e Å^{-3}) was below the usually employed 1-*e* Å^{-3} threshold for reporting and located at the coordinates [x, y, z] = [0.3771, 0.5585, 0.9631], which is 1.395 Å from Pt1B.

3.1.2. General spectroscopy

Proton (^{1}H) and carbon (^{13}C) NMR spectra were recorded on Bruker Avance III 400 and 300 NMR spectrometers at ^{1}H frequencies of 400 MHz and 300 MHz, respectively, and ^{13}C frequencies of 100 MHz and 75 MHz, respectively. Spectra were recorded at 300 K with 5 mm BBOZ or TBIZ probes. Chemical shifts for both proton and carbon were referenced using the solvent signal. MestReNova (version 14.2.1-27684) was used to analyse all NMR spectra.

FTIR spectra of powder samples were recorded using a Bruker Alpha FTIR spectrometer incorporating a Bruker Platinum diamond ATR sampling accessory. Spectra were analysed using the OPUS software package on the spectrometer (version 7.5).

Electronic spectra were recorded using either a PerkinElmer Lambda 365 double-beam spectrometer connected to a Peltier controller and a Peltier Temp multicell thermostatic cell block or an Analytik Jena Specord210 Plus double-beam instrument fitted with external water circulating thermostatic bath and thermostatic cell holders. The spectral data were analysed with the spectrometer software or Origin Pro 2020. Spectra were recorded as a function of concentration for both characterization and the determination of molar absorptivity constants. Quartz cuvettes with a path length of 10 mm were used.

4. Compound synthesis

4.1.1. Ligand synthesis

1,3-bis{[(1*E*)-1*H*-pyrrol-2-ylmethylene]amino}propan-2-ol (H_2(OH)Pyrr). In brief, the synthesis of H_2(OH)Pyrr involved refluxing pyrrole-2-carboxaldehyde (0.5706 g; 6 mmol) with 1,3-diamino propanol (0.2704 g; 3 mmol) for 2 hours in ethanol (30 mL) in which time the solution changed from colourless to bright orange. The ligand was precipitated out by overnight evaporation of ethanol.

2,2-dimethyl-*N*,*N*'-bis[(1*E*)-1*H*-pyrrol-2-ylmethylene]propane-1,3-diamine ($H_2(CH_3)_2$Pyrr). In brief was synthesized by refluxing pyrrole-2-carboxaldehyde (0.5705 g, 6 mmol), and 1,3-diamino-2,2-dimethyl propane (0.3066 g, 3 mmol) was refluxed in ethanol (30 mL) for one hour. The solution changed from colourless to orange. The ligand was precipitated out by overnight evaporation of the ethanol.

(1*S*,2*S*)-*N*,*N*'-bis[(1*E*)-1*H*-pyrrol-2-ylmethylene] cyclohexane -1,2-diamine (H_2(-S-cyclohexane)Pyrr). The enantiomerically pure ligand was synthesized by a solid-state reaction using the enantiomerically pure (1S, 2S) cyclohexane diamine (0.303 g, 2.65 mmol) with an agate pestle and mortar with pyrrole-2-carboxaldehyde (0.500 g, 5.30 mmol) for between 10 to 15 minutes until a brown oil was formed. The brown oil was dissolved in dichloromethane and

dried with $MgSO_4$ to remove the water from the condensation reaction. The solution was filtered through celite before being layered with hexane, which yielded thin white rod-shaped crystals.

4.1.2. Synthesis of Pt(II) bis(pyrrolide-imine) chelates

2,2'-{(2-hydroxypropane-1,3-diyl)bis[nitrilo(*E*) methylylidene]} bis(pyrrol-1-ido) platinum(II) (**1**) and 2,2'-{(2,2-dimethylpropane-1,3-diyl)bis[nitrilo(*E*)methylylidene]} bis(pyrrol-1-ido) platinum(II) (**2**), were prepared in a similar manner.[4] To a round bottom flask either H_2(OH)Pyrr (100 mg, 0.410 mmol) or $H_2(CH_3)_2$Pyrr (100 mg, 0.393 mmol) were added to 15 mL of DMF containing 2-mole equivalents of sodium acetate and the solution was heated to 80 °C. Thereafter, K_2PtCl_4 was dissolved in 15 mL of DMSO, and K_2PtCl_4 (0.410 mmol, 0.170 g) was added to the H_2(OH)Pyrr solution, while K_2PtCl_4 (0.393 mmol, 0.163 g) was similarly added to the $H_2(CH_3)_2$Pyrr solution. The solutions were then stirred at 80 °C for a further 4 h. A colour change from yellow to dark orange over time indicated spectral changes consistent with metalation and thus the formation of the target Pt(II) bis(pyrrolide-imine) chelates.

1 was water soluble. Therefore, 100 mL of cold distilled H_2O was added to the 50% (V/V) DMSO:DMF solution, which was then placed in a separating funnel. **1** was then extracted from the aqueous (DMSO:DMF) layer with ethyl acetate (5 x 250 mL). The solution was then concentrated by rotary evaporation. Red crystals suitable for X-ray diffraction were obtained by slow liquid diffusion of ether into the ethyl acetate solution of **1**.

2 was precipitated by adding 100 mL of cold distilled H_2O, and the solution was filtered by gravity filtration leaving a yellow precipitate behind. The yellow precipitate was dried overnight and then dissolved in DCM (~30 mL). DCM was removed by rotary evaporation at 40 °C, upon removal of DCM single red crystals suitable for X-ray diffraction of **2** formed.

4.1.3. Characterization of bis(pyrrolide-imine) ligands

1,3-bis{[(1*E*)-1*H*-pyrrol-2-ylmethylene]amino}propan-2-ol (H_2(OH)Pyrr). The ligand was analysed by ^{1}H NMR, ^{13}C NMR, FT-IR, and UV-visible spectroscopy. ^{1}H NMR (400 MHz, DMSO-d_6-300 K) [δ, ppm]: 3.43 (dd, *J* = 11.7, 6.5 Hz, 2H, CH_2-N=CH), 3.77 – 3.54 (m, 2H, CH_2-N=CH), 4.00 – 3.82 (m, 1H, H-7), 6.11 (t, *J* = 3.0 Hz, 2H, H-2), 6.44 (dd, *J* = 3.5, 1.5 Hz, 2H, H-3), 6.87 (t, *J* = 1.9 Hz, 2H, H-1), 8.07 (s, 2H, H-5), 11.34 (s br, 2H, DMSO-d_6 exchangeable, H-9). ^{13}C NMR (101 MHz, DMSO-d_6, 300 K) [δ, ppm]: 65.14 (C-6), 70.69 (C-7), 108.98 (C-2), 113.35 (C-3), 122.03 (C-1), 130.41 (C-4), 152.92 (C-5). IR (KBr pellet, cm^{-1}): 3254w (NH, pyrrole), 3088m (CH, imine), 2882 (CH, H-COH), 2859 (CH, CH_2-N=CH), 1633s (C=N), 1127 (C-O stretch). UV/vis (ethanol) [λ, max, nm; ε, mol^{-1} dm^3 cm^{-1}]: 289; 3.23 × 10^4.

2,2-dimethyl-*N*,*N*'-bis[(1*E*)-1*H*-pyrrol-2-ylmethylene]propane-1,3-diamine ($H_2(CH_3)_2$Pyrr). The ligand was analysed by ^{1}H NMR, ^{13}C NMR, FT-IR, and UV-Visible spectroscopy. ^{1}H NMR (400 MHz, Chloroform-*d*, 300 K) [δ, ppm]: 0.97 (t, *J* = 4.3 Hz, 6H, H-8), 3.46 (t, *J* = 4.2 Hz, 4H, H-6), 6.26 (p, *J* = 3.2 Hz, 2H, H-2), 6.48 (dt, *J* = 6.6, 3.4 Hz, 2H, H-3), 6.90 (d, *J* = 6.1 Hz, 2H, H-1), 7.99 (t, *J* = 4.2 Hz, 2H, H-5), 9.50 (s br, 2H, H-9). ^{13}C NMR (101 MHz, Chloroform-*d* 300 K) [δ, ppm]: 24.28

(C-8), 36.96 (C-7), 69.32 (C-6), 109.44 (C-2), 114.28 (C-3), 122.20 (C-1), 130.06 (C-4), 152.17 (C-5). FT-IR (KBr pellet, cm^{-1}): 3130m br *v*(CH, imine), 2966m *v*(CH, terminal CH_3), 2852m *v*(CH_2, alkyl), 1635s br *v*(C=N). UV-vis (ethanol) [λ, max, nm; ε, mol^{-1} dm^3 cm^{-1}]: 289; 3.23 × 10^4.

(1*S*,2*S*)-*N*,*N*'-bis[(1*E*)-1*H*-pyrrol-2-ylmethylene] cyclohexane -1,2-diamine (H_2(-S-cyclohexane)Pyrr). The ligand was analysed by ^{1}H NMR (400 MHz, DMSO-d_6, 300 K) [δ, ppm]: 1.34 – 1.80 (m, 8H, H-7, and H-8), 3.23 (m, 2H, H-6), 6.01 (t, *J* = 3.0 Hz, 2H, H-2), 6.31(dd, $^3J_1$ = 3.5 Hz, $^3J_2$ 1.4 Hz, 2H, H-3), 6.76 (t, *J* = 1.9 Hz, 2H, H-1), 7.94 (s, 2H, H-5), 11.16 (s, 2H, H-9). ^{13}C NMR (101 MHz, DMSO-d_6, 298 K) [δ, ppm]: 24.70 (C-8), 33.85 (C-7), 74.09 (C-6), 109.07 (C-2), 113.61 (C-3), 122.08 (C-1), 130.33 (C-4), 151.26 (C-5). UV-vis (acetonitrile) [λ, max, nm; ε, mol^{-1} dm^3 cm^{-1}]: 289; 2.37 x 10^4.

4.1.4. Characterization of Pt(II) bis(pyrrolide-imine) chelates

2,2'-{(2-hydroxypropane-1,3-diyl)bis[nitrilo(*E*) methylylidene]} bis(pyrrol-1-ido) platinum(II) (1). ^{1}H NMR (400 MHz, DMSO-d_6) δ 8.19 (s, 1H; H16), 7.20 (s, 2H; H5), 6.65 (d, *J* = 3.8 Hz, 2H; H1), 6.17 (dd, *J* = 3.8, 1.9 Hz, 2H; H3), 5.30 (d, *J* = 4.5 Hz, 1H; H21), 4.03 – 3.95 (m, 2H; H20), 3.82 (d, *J* = 14.0 Hz, 2H; H18 equatorial), 3.66 (dd, *J* = 14.1, 7.6 Hz, 2H; H18 axial). ^{13}C NMR (101 MHz, DMSO-d_6) δ 161.75 (C6), 140.88 (C2), 135.52 (C5), 117.25 (C1), 110.84 (C3), 70.47 (C20), 59.76 (C18). IR (KBr pellet, cm^{-1}): 3083 (CH, imine), 2990 (CH, H-COH), 2904 (CH, CH_2-N=CH), 1575 (C=N), 1126 (C-O stretch). [λ_{max}/nm, ε/mol^{-1} dm^3 cm^{-1} (CH_3CN)]: 277, 1.64 × 10^4; 303, 1.91 × 10^4; 313, 2.11 × 10^4; 382, 1.55 × 10^4.

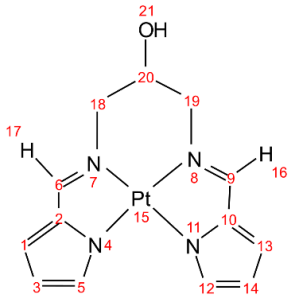

2,2'-{(2,2-dimethylpropane-1,3-diyl)bis[nitrilo(*E*)methylylidene]} bis(pyrrol-1-ido) platinum(II) (2). ^{1}H NMR (400 MHz, DMSO-d_6) δ 8.16 (s, 2H; H1), 7.21 (s, 2H; H5), 6.66 (d, *J* = 3.8 Hz, 2H; H7), 6.18 (dd, *J* = 3.9, 1.9 Hz, 2H; H6), 3.48 (s, 4H; H16), 1.05 (s, 6H; H19). ^{13}C NMR (101 MHz, DMSO-d_6) δ 161.23 (C2), 140.78 (C3), 135.44 (C5), 117.21 (C7), 110.88 (C6), 64.52 (C16), 38.78 (C17), 23.90 (C19). IR (KBr pellet, cm^{-1}): 3085 (CH, imine), 3015m (CH, terminal CH_3), 2933 (CH_2, alkyl), 1652 (C=N). IR (cm^{-1}): 2919m br *v*(CH, imine), 1566s br *v*(C=N). [λ_{max}/nm, ε/mol^{-1} dm^3 cm^{-1} (CH_3CN)]: 277, 1.64 × 10^4; 303, 1.85 × 10^4; 313, 2.06 × 10^4; 382, 1.51 × 10^4.

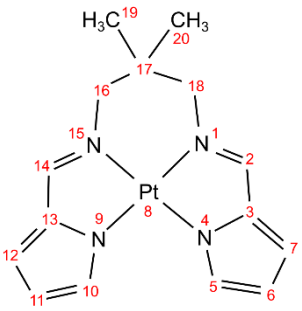

2,2'-{(1*S*,2*S*)-cyclohexane-1,2-diylbis[nitrilo(*E*)methylylidene]}bis(pyrrol-1-ido)platinum(II) (3). ^{1}H NMR (400 MHz, DMSO-d_6) δ 8.15 (s, 2H; H8/H20), 7.10 (s, 3H; H12/H17), 6.64 (d, *J* = 3.8 Hz, 3H; H10/H15), 6.14 (dd, *J* = 3.9, 1.8 Hz, 3H; H11/H16), 3.92 (d, *J* = 8.6 Hz, 2H, H1′/H4′ eq), 3.17 (d, *J* = 4.3 Hz, 2H, H5/H6), 1.75 (d, *J* = 8.9 Hz, 2H, H2′/3′ eq), 1.49 (m, 2H, H2/H3 ax), 1.34 (t, *J* = 10.4 Hz, 2H, H1/H4 ax). ^{13}C NMR (101 MHz, DMSO-d_6) δ 152.99 (C8/C20), 144.32 (C12/C17), 135.92 (C9/C19), 117.61 (C10/C15), 109.38 (C11/C16), 73.06 (C5/C6), 26.99 (C1/C4), 23.24

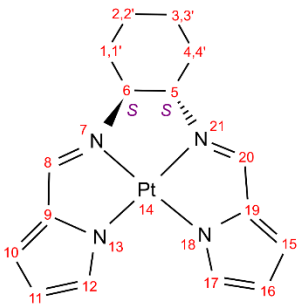

(C2/C3). IR (cm^{-1}): 2945m br *ν*(CH, imine), 1564s br *ν*(C=N). [λ_{max}/nm, ε/mol^{-1} dm^3 cm^{-1} (CH_3CN)]: 277, 1.89 × 10^4; 303, 1.73 × 10^4; 316, 1.89 × 10^4; 382, 2.04 × 10^4.

5. Fluorescence and CD spectroscopy

5.1.1. Steady state fluorescence

Pt(II) bis(pyrrolide-imine) chelates binding to and quenching HSA fluorescence. Pt(II) bis(pyrrolide-imine) chelates (0 – 1.24 x 10^{-5} M in DMSO) were titrated into a solution of HSA (5 x 10^{-6} M) in KH_2PO_4 buffer (50 x 10^{-6} M, pH7.5). The excitation slit width was 5 nm and the emission slit width was 10 nm. The protein was excited at 282 nm and the fluorescence emission was measured from 310 nm to 400 nm for all temperatures.

Fluorescent probe displacement assay. Warfarin and ibuprofen were used as fluorescent site-specific marker probes for Sudlow's sites I and II, respectively. Steady-state fluorescence spectra were recorded as described above at 298 K using 10 nm excitation and emission bandwidths for warfarin, while 5 nm excitation and 10 nm emission bandwidths were employed for ibuprofen. The fluorophores warfarin and ibuprofen were equilibrated (bound) to HSA (50 mM KH_2PO_4 buffer, pH 7.50) and were excited at 320 nm and 228 nm, respectively. The emission spectrum was measured in the range of 350 – 500 nm for warfarin and 228 – 450 nm for ibuprofen. The HSA and fluorescence probe concentrations were both used at 5.0 μM. Titrations were performed by increasing the concentrations of the Pt(II) bis(pyrollide-imine) chelates in the protein-probe solution from 0 to 25.9 μM.

Correction of fluorescence data. Inner filter effect (IFE) correction was applied to all fluorescence data using eq. S1.[5]

$$F_{corrected} = F_{observed} * 10^{Aex*dex+Aem*dem} \qquad \text{S1}$$

Where $A_{excited}$ and $A_{emission}$ are the absorbance reading at the excitation and emission wavelengths. While d is the path length of the cuvette.

Further corrections were applied to the concentration of the ligand. i.e., if $[Ligand]_{added}$ was not equal to $[Ligand]_{free}$, the free ligand concentration was calculated using eq. S2[6]

$$[Ligand]_{free} = [Ligand]_{added} - \frac{F_o}{F_o} - \frac{F}{F_c} * [HSA] \qquad \text{S2}$$

5.1.2. UV and UV-vis circular dichroism (CD)

General CD spectroscopy. Far-UV CD spectra of solutions of HSA (3.0 × 10^{-7} mol dm^{-3}) in the absence and presence of increasing concentrations (0–40 μM) of Pt(II) bis(pyrrolide-imine) chelates were recorded with a JASCO J-1500 CD spectrometer equipped with a Peltier temperature controller (25 °C). A scan speed of 100 nm min^{-1} was employed for spectral acquisition with a 0.5 nm data pitch and a response time of 2 s. Each spectrum was the average of three scans. Spectra were recorded over a wavelength range of 200–260 nm (0.4 cm pathlength quartz cuvette). All spectra were processed with JASCO Spectral Manager™.

Near-UV region CD spectra (250–310 nm, 1.0-cm pathlength quartz cuvette, 25 °C) and UV-vis CD spectra (300–500 nm, 1.0-cm pathlength quartz cuvette, 25 °C) were recorded similarly to detect induced CD (ICD) signals of the achiral ligands and Pt(II) metal chelates upon their uptake by HSA. Typically, HSA (15×10^{-6} M) was incubated (25 °C) with one molar equivalent of the Pt(II) bis(pyrrolide-imine) chelates for at least 60 min in 50 mM KH_2PO_4 buffer at pH 7.5. A scan speed of 50 nm min^{-1} was used with a 0.5-nm data pitch (response time, 2 s) for the near UV-vis CD spectrum and 100 nm min^{-1} for the UV-vis CD spectrum; each spectrum was the average of three scans.

Site displacement assay by UV-vis CD spectroscopy. Typically, two cuvettes were set up with HSA in buffer (15×10^{-6} M) and incubated with one molar equivalent of the candidate Pt(II) bis(pyrrolide-imine) chelate for at least 60 min in 50 mM KH_2PO_4 buffer at pH 7.5 (25 °C). A scan speed of 50 nm min^{-1} was used with a 0.5-nm data pitch (response time, 2 s) for the near-UV CD spectra and 100 nm min^{-1} for the UV-vis CD spectra; each spectrum was the average of three scans. Thereafter, two site-specific markers, namely warfarin (Sudlow's site I) or ibuprofen (Sudlow's site II), were titrated into the solution; spectra were recorded as above after each aliquot of titrant added had been equilibrated in the reaction solution for 10 minutes.

Analysis of CD spectra to determine secondary structure composition. We utilised the JWMVS-529 Protein Secondary Structure Analysis program, incorporated in JASCO's Spectra Manager™ package, to analyse the secondary structure composition of HSA based on the recorded CD spectra. This program employs a library of 26 protein CD spectra (176–260 nm) provided by JASCO to establish a calibration model.[7] By applying the partial least squares (PLS) method and principal component regression (PCR) techniques,[8] the experimental CD spectra were fitted to the calibration model, allowing for accurate estimation of the fractional composition of α-helix, β-sheet, turn, and unordered coil structures. Notably, this approach significantly enhances the assessment of β-sheet motifs, which lack strong specific CD marker bands. We opted for these methods over an older algorithm, the JWSSE-513 Protein Secondary Structure Analysis program, offered by JASCO, which employs a classical least squares (CLS) fitting algorithm based on the reference spectra set of Yang et al.[9] Although other methods for protein secondary structure prediction can be found in the literature, we did not utilize them in this study as suitable methods were readily available in JASCO's Spectra Manager™ package on the spectrometer's controlling computer.[10,11]

Solution stability assays. To understand the kinetic behaviour of metal chelates **1**–**3** in solutions of similar or identical composition to those used for protein binding determinations, spectra of the Pt(II) chelates were recorded as a function of time in the absence of the protein. Specifically, the three Pt(II) chelates were diluted from DMSO stock solutions into solutions of KH_2PO_4 buffer (50 mM, pH 7.5). The final solution of **1** (hydroxy derivative) had less than 1% (V/V) DMSO after dilution while the solutions of

complexes **2** and **3** each contained 20% (V/V) DMSO after dilution (with [Pt] = 20 µM after dilution in all cases). The UV-vis spectra of **1** and **2** were recorded hourly over a period of 24 hours, while spectra for **3** were recorded over a period of 240 min due to precipitation problems. Only data acquired over periods of constant baseline intensity were used for final spectral processing and plotting.

6. Molecular simulations

All *in silico* studies were carried out as reported by Sookai and Munro.[12] The methods are reiterated briefly below.

6.1.1. DFT Calculations

Simulations were performed to calculate optimized structures, vibrational frequencies, and electronic spectra for Pt(II) chelates **1** and **2** using Gaussian 16 Rev C.01[13] at the CAM-B3LYP[14]/DEF2-QZVP[15] level of theory using the GD3BJ empirical dispersion correction.[16] Structures were also calculated using the SDD basis set.[17] The default geometry convergence criteria in Gaussian 16 were applied. Nuclear shielding tensors were calculated by the default GIAO method[18,19] in Gaussian. Input Pt(II) chelate structures were derived from the X-ray structure atomic coordinates (C_1 symmetry). Simulations were carried out *in vacuo* and in acetonitrile, DMSO, and water solvent continua (SCRF PCM method[20]). GaussView 6.0.16[21] was used for preparing input files and data visualization. GaussSum 3.0 was used to visualize electronic spectra and tabulate transition assignments.[22] All geometry-optimized structures were characterized by positive frequency eigenvalues, indicating that true minima were located on the global potential energy surface for each system.

Time-dependent DFT (TD-DFT) simulations were carried out using the above method (CAM-B3LYP) and basis sets in Gaussian 16 for all small molecules. Typically, 60 excited singlet states were computed to cover the full spectral range (150–900 nm). TD-DFT simulations on protein complexes required the use of the ONIOM[23] method employing two layers: a high or quantum mechanical (QM) layer computed at the CAM-B3LYP/SDD/GD3BJ level of theory and a low layer (molecular mechanics) calculated using the UFF[24] force field. The input structures for the single-point calculations were derived from the best-scoring poses of the ligands of interest docked within the relevant binding site in HSA taken directly from the output of a GLIDE XP[25] docking run with the relevant X-ray structure target (e.g., PDB code: 2BXF). For the QM layer of HSA•{**1**}, all atoms of the metal chelate were included at the high level. Three amino acid side chains (Ile-388, Phe-403, Leu-407 Arg-485, and Tyr-411) were included in the QM layer around **1** located within Sudlow's site II in the simulations for HSA•{**1**} to achieve an electronic structure that best-matched experiment, specifically the calculated CD spectrum of the macromolecular complex. This is illustrated in the two boxes below.

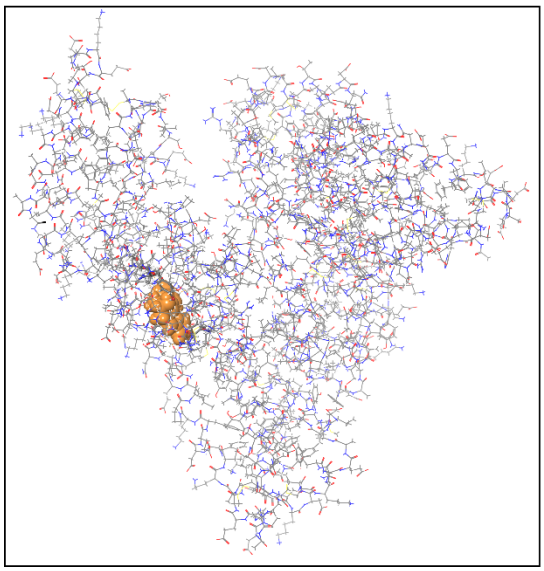

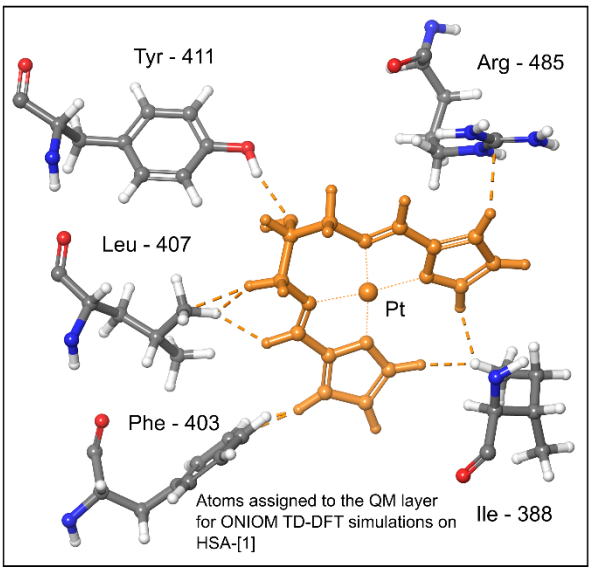

6.1.2. Molecular Docking Simulations

System preparation. The 2.5-Å and 2.95-Å X-ray crystal structures of HSA in complex with warfarin,[26] diazepam,[27] and ibuprofen[27] were retrieved from the Protein Data Bank (PDB ID codes: 1HA2, 2BXF, and 2BXG). The structure of HSA was pre-processed, minimized, and refined using the Protein Preparation Wizard[28] employed in Schrödinger Suite 2022-3. This step included eliminating crystallographic waters within 5 Å of the ligand binding site, adding missing hydrogen atoms and side chain atoms, as well as assigning the appropriate charge and protonation state of the receptor structure (pH = 7.4) using Prime. Finally, the protein structure was subjected to energy minimization using Macromodel[29] and the S-OPLS force-field[30,31] with a RMSD cut-off value of 0.30 Å to resolve steric clashes among closely spaced residues arising from the addition of hydrogen atoms.

The structures of Pt(II) complexes **1** and **2** for docking inputs were obtained by DFT simulations at the CAM-B3LYP/DEF2-QZVP level of theory in a water solvent continuum (SCRF PCM model) and implementing the GD3BJ empirical dispersion energy correction. Minor adjustments were required to prepare the metal chelate structures for docking with GLIDE. First, the metal was given a +2 charge and the pyrrole nitrogen atoms were each given a −1 charge. Second, the bonds from the four N-donor atoms to the metal ion were assigned bond orders of zero. This step is mandatory as it obviates the need for specific force field parameters involving the metal ion; the coordination geometry is then restrained to remain similar to the input DFT-calculated geometry by GLIDE during optimization and fitting. Lastly, partial charges were assigned to the structures using the S-OPLS force-field.

Molecular docking. Docking was performed with GLIDE[25,32,33] to identify the best-fit orientation of the compounds (ligands) into both Sudlow's site I (exemplified by PDB code 1HA2) or Sudlow's site II (PDB code 2BXF) and any sites within ~20 Å of each site.[34] The appropriate hard receptor grid was generated based upon a set of centre coordinates using a cube with dimensions 40 × 40 × 40 Å^3 in each case. The grid box employed was a factor of 4 times larger than the default box size (10 × 10 × 10 Å^3) and centred on the centroid of the relevant HSA-bound drug (warfarin or diazepam) or protein residue (typically Trp-214). The drug was then automatically removed prior to grid generation. This strategy was adopted because the metal chelates are slightly larger than the typical small molecule drugs bound in Sudlow's sites I and II and we wanted to ensure appropriate sampling of any atypical binding sites close to the main drug-binding pockets.

The metal chelates and free ligand species were then flexibly docked into the relevant binding site grids using the extra precision (XP) docking protocols of GLIDE; aromatic hydrogens were included as H-bond donors. The best-scoring pose for each compound with each PDB structure of native HSA was saved and selected for further analysis.

Docking simulations on HSA targets containing pre-bound drugs (warfarin, diazepam, and ibuprofen) were also performed to evaluate the ability of the protein to take up the metal chelates at binding site locations close to the bound drugs as well as secondary sites located further away. These experiments were performed as described above with grids centred on Trp-214 at the core of the protein. The ligand/drug present in the X-ray structure was retained when setting up the receptor grid. These unconventional experiments were specifically aimed at understanding our fluorescence titration data for HSA pre-equilibrated with warfarin and ibuprofen.

7. Figures

7.1.1. Ligand structures

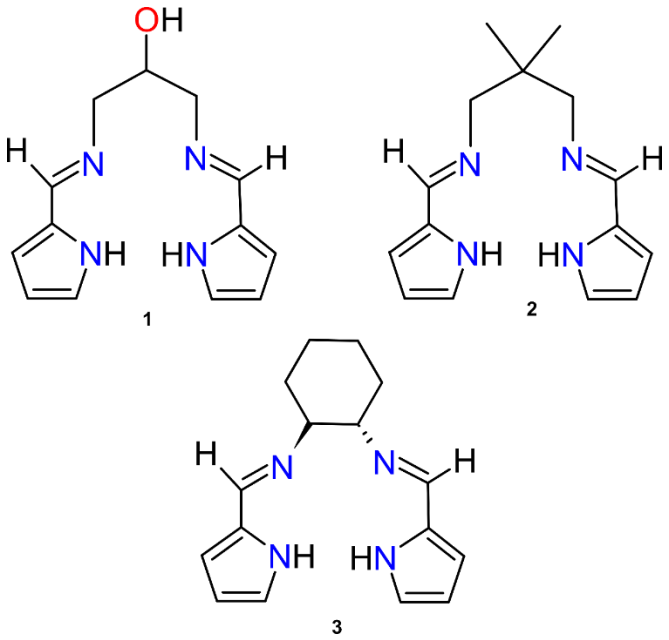

Fig. S1. Structures of the bis(pyrrole-imine) ligands synthesized and used in this study to chelate Pt(II): 1,3-bis(*E*){[(1*H*-pyrrol-2-yl)methylidene]amino}propan-2-ol, **1**, (*E*,*E*)-*N*,*N*'-(2,2-dimethylpropane-1,3-diyl)bis[1-(1*H*-pyrrol-2-yl)methanimine], **2**, and (*E*,*E*)-*N*,*N*'-[(1*S*)-cyclohexane-1,2-diyl]bis[1-(1*H*-pyrrol-2-yl)methanimine], **3**.

7.1.2. NMR, IR, and UV-vis spectra

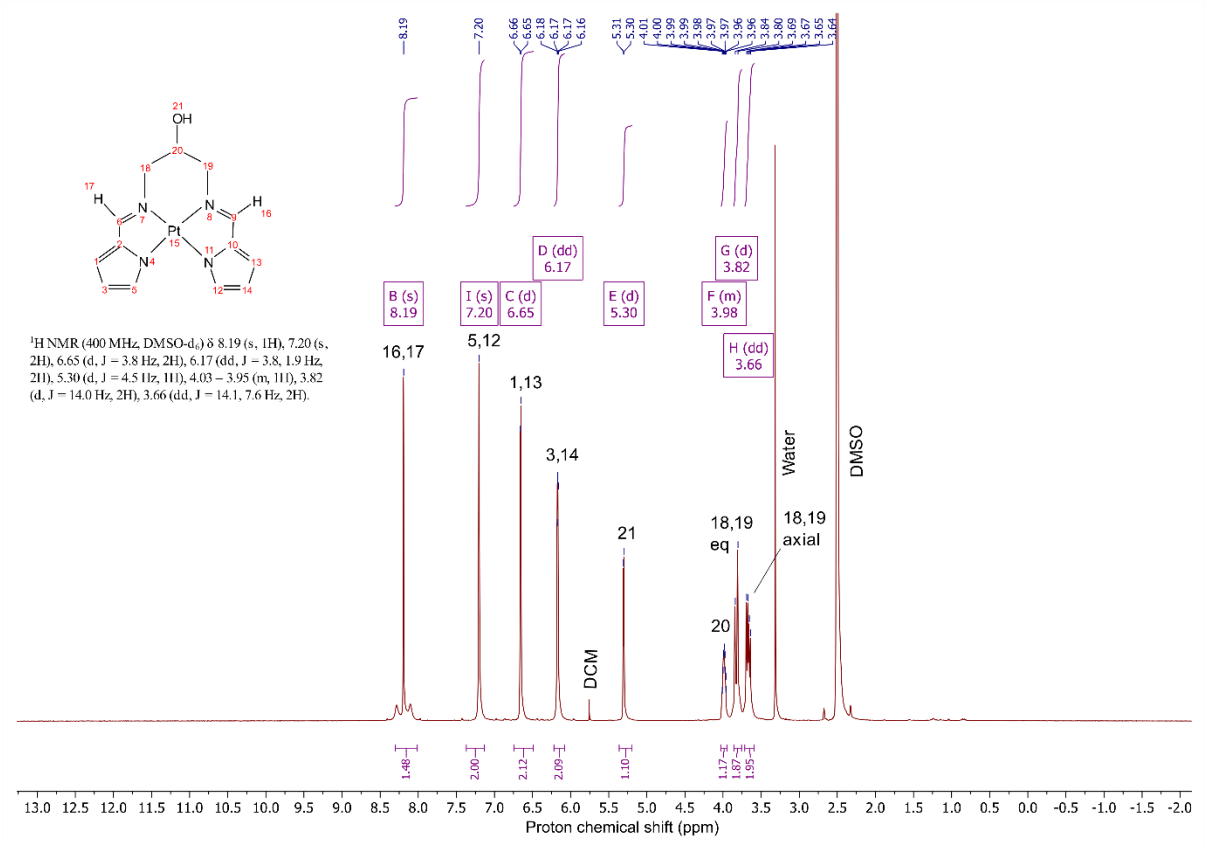

Fig. S2 400 MHz ^{1}H NMR spectrum of **1** recorded in DMSO-d_6 at 300 K.

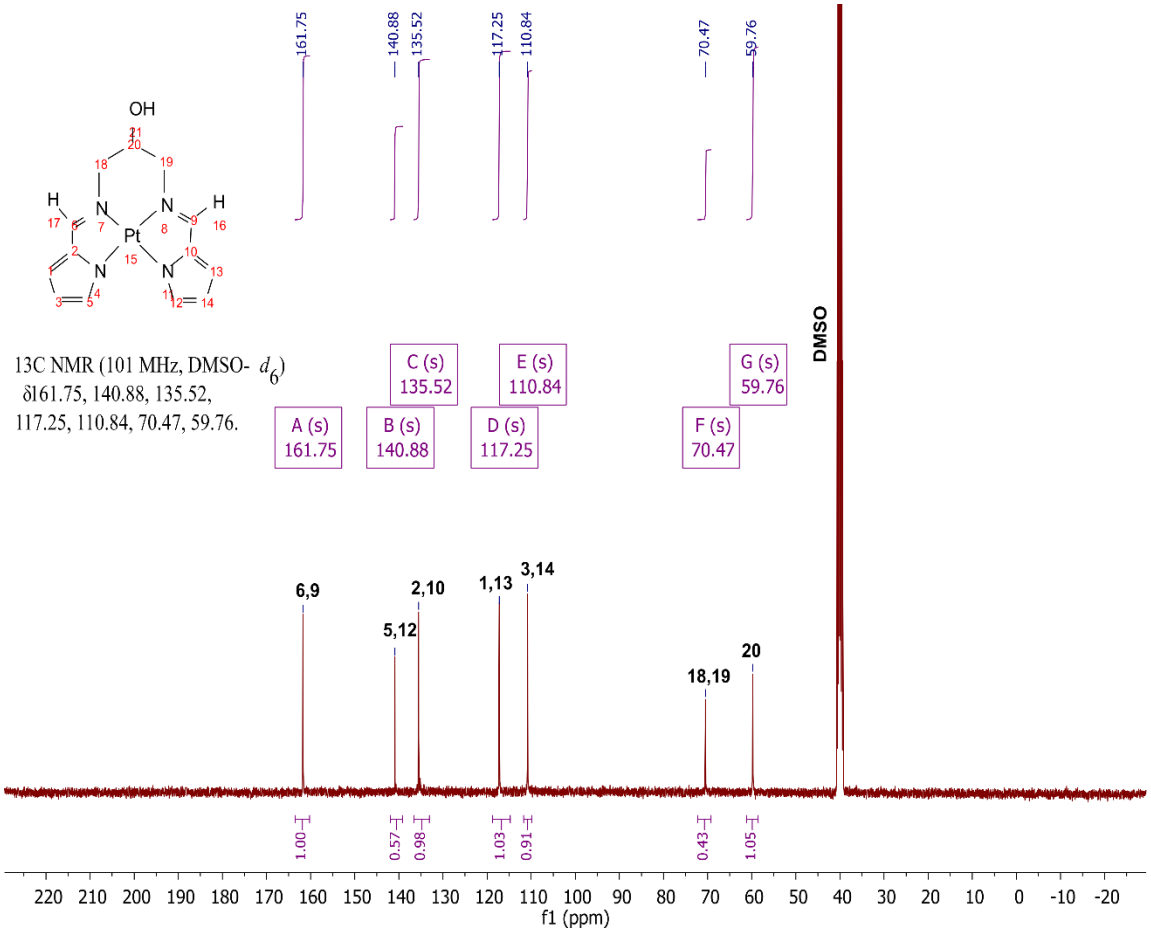

Fig. S3 101 MHz ^{13}C NMR spectrum of **1** recorded in DMSO-d_6 at 300 K.

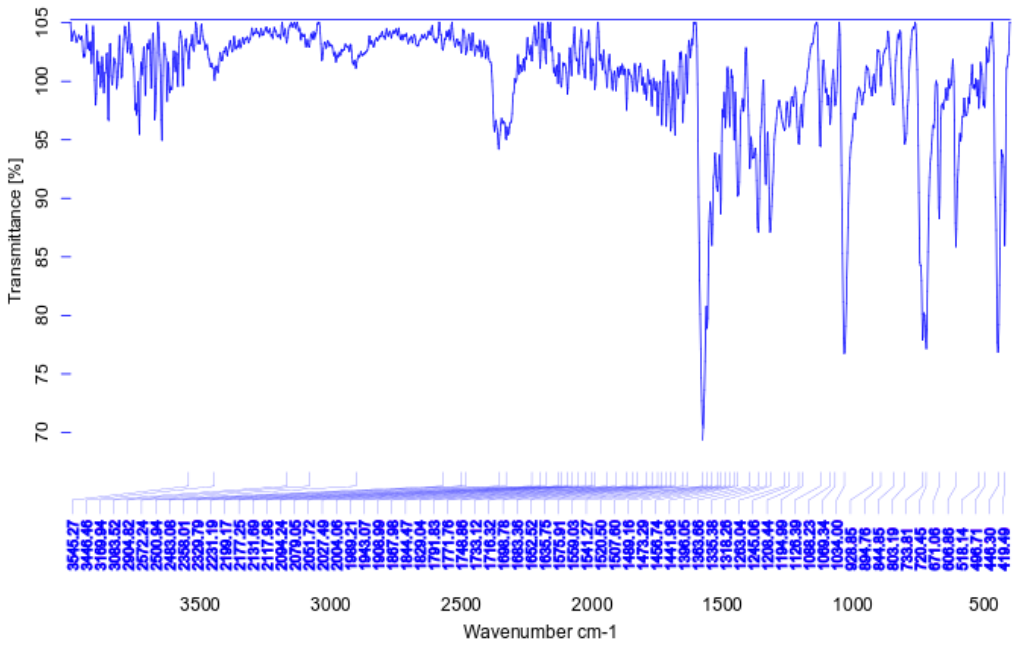

Fig S4. FTIR spectrum of **1** recorded as a crushed powder sample at 295 K.

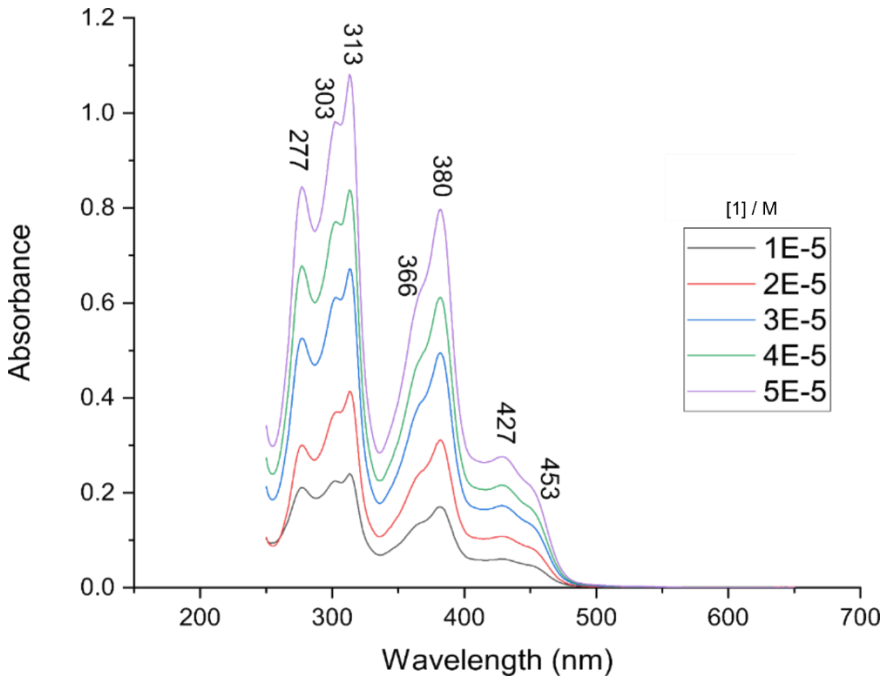

Fig. S5 UV-visible spectrum of **1** recorded in acetonitrile at 295 K as a function of concentration. The molar absorptivities of key band maximum are reported in Section 4 and were determined from the slopes of Beer-Lambert law plots at the relevant band maxima.

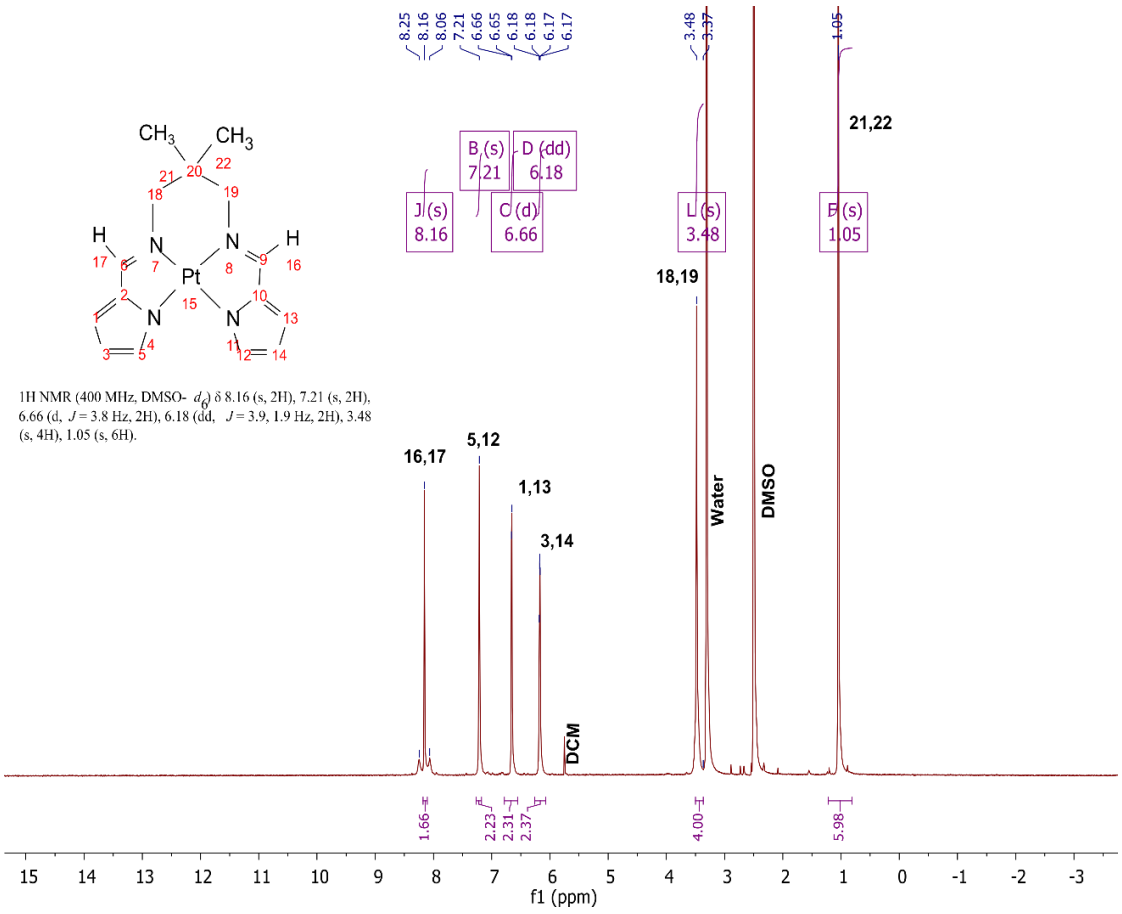

Fig. S6 400 MHz ^{1}H NMR spectrum of **2** recorded in DMSO-d_6 at 300 K.

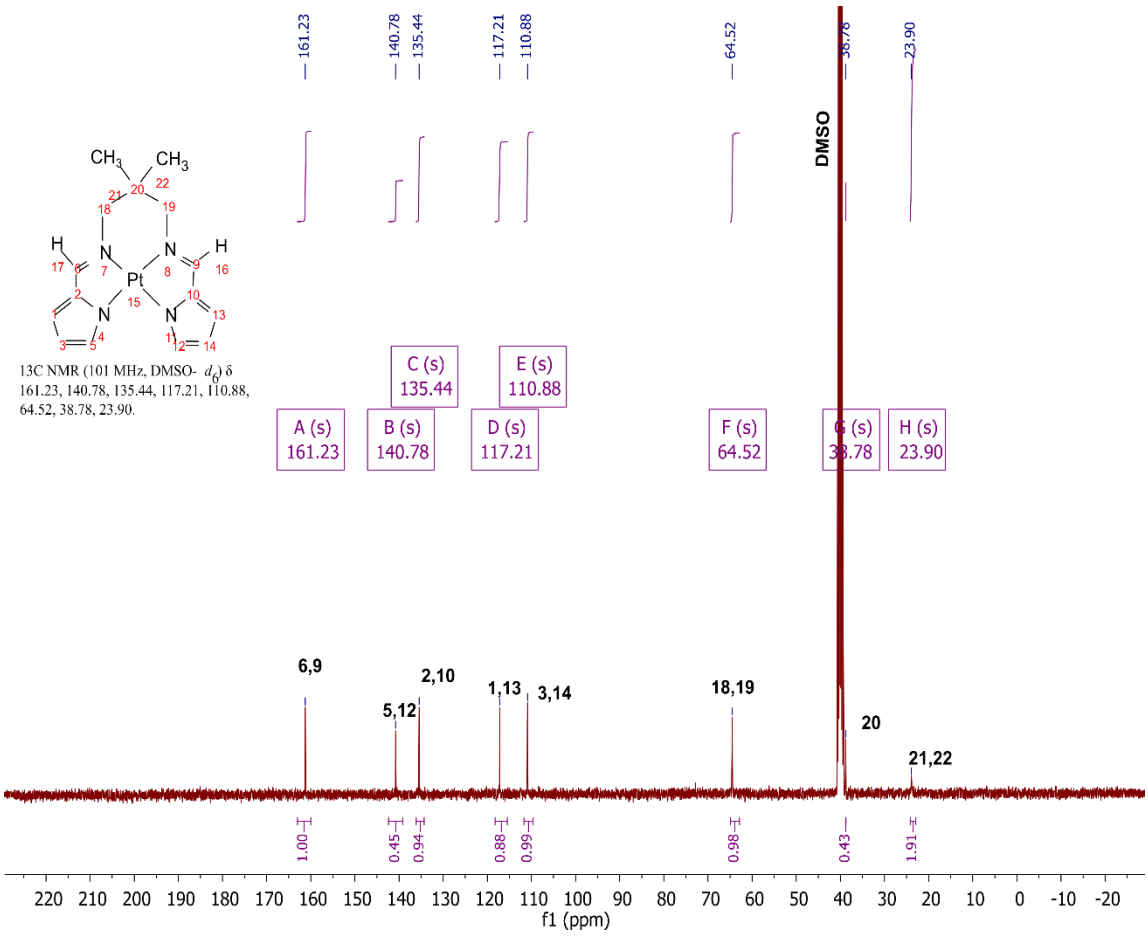

Fig. S7 101 MHz ^{13}C NMR spectrum of **2** recorded in DMSO-*d*6 at 300 K.

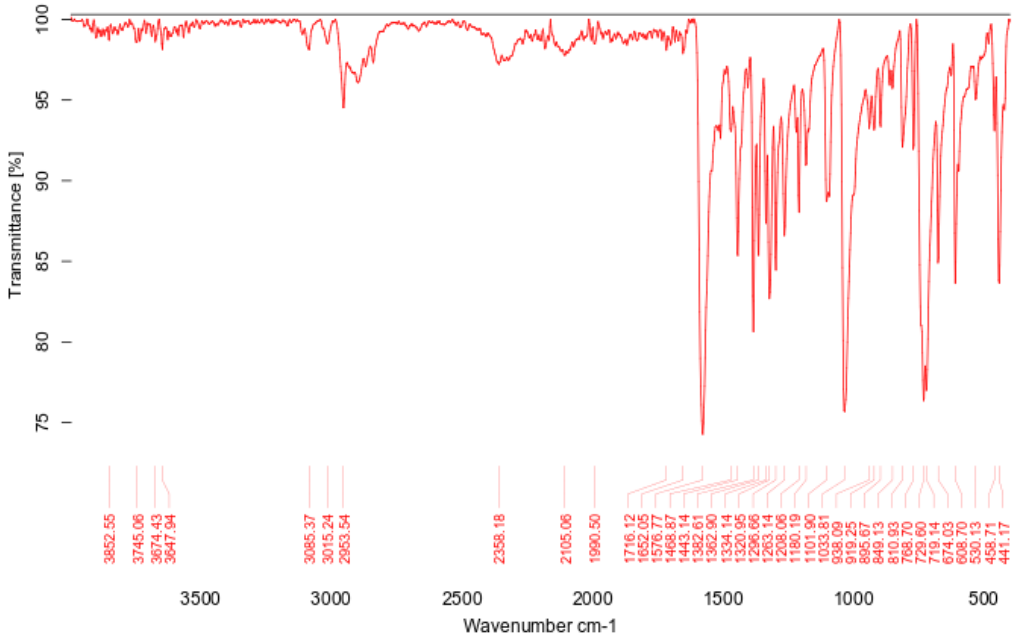

Fig. S8 FTIR spectrum of **2** recorded as a crushed powder sample at 295 K.

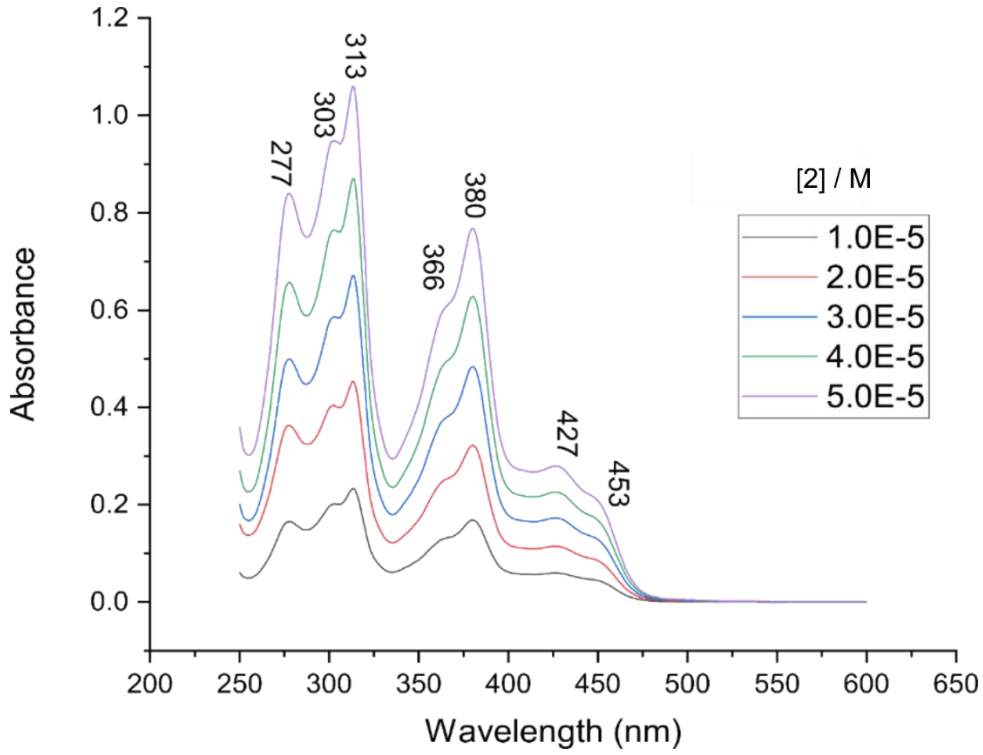

Fig. S9 UV-visible spectrum of **2** recorded in acetonitrile at 295 K as a function of concentration. The molar absorptivities of key band maximum are reported in Section 4 and were determined from the slopes of Beer-Lambert law plots at the relevant band maxima.

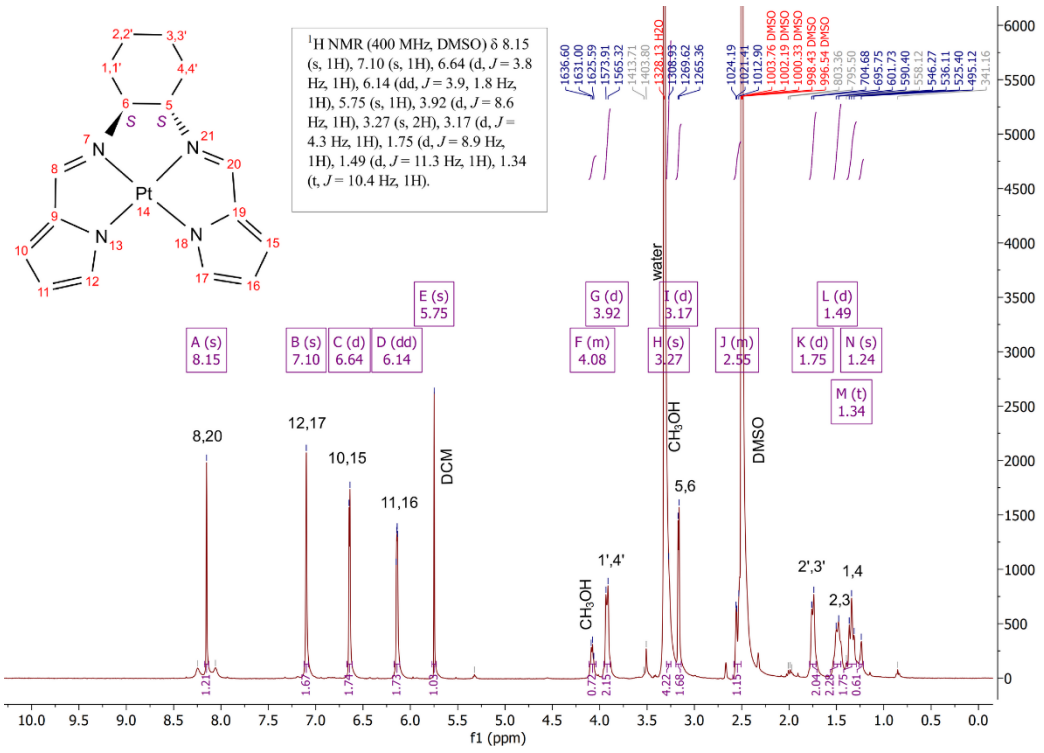

Fig. S10 400 MHz ^{1}H NMR spectrum of **3** recorded in DMSO-d_6 at 300 K. This compound is known;[4] the spectral data here briefly confirm the structure of the compound and its purity.

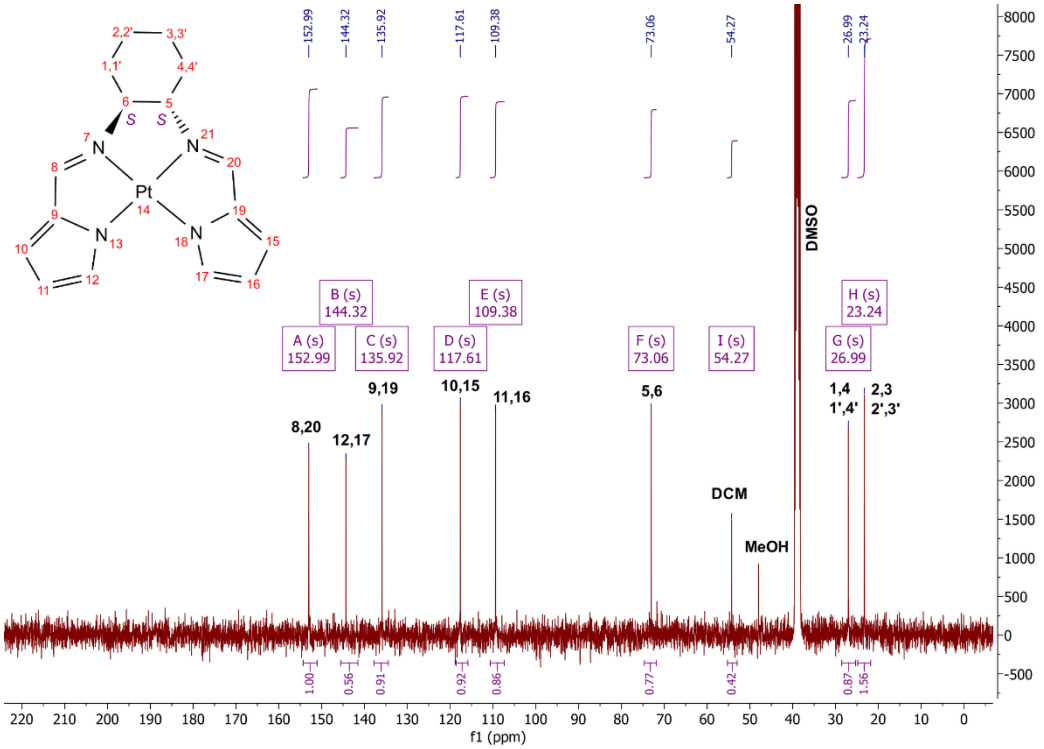

Fig. S11 101 MHz ^{13}C NMR spectrum of **3** recorded in DMSO-d_6 at 300 K.

7.1.3. X-ray crystallography

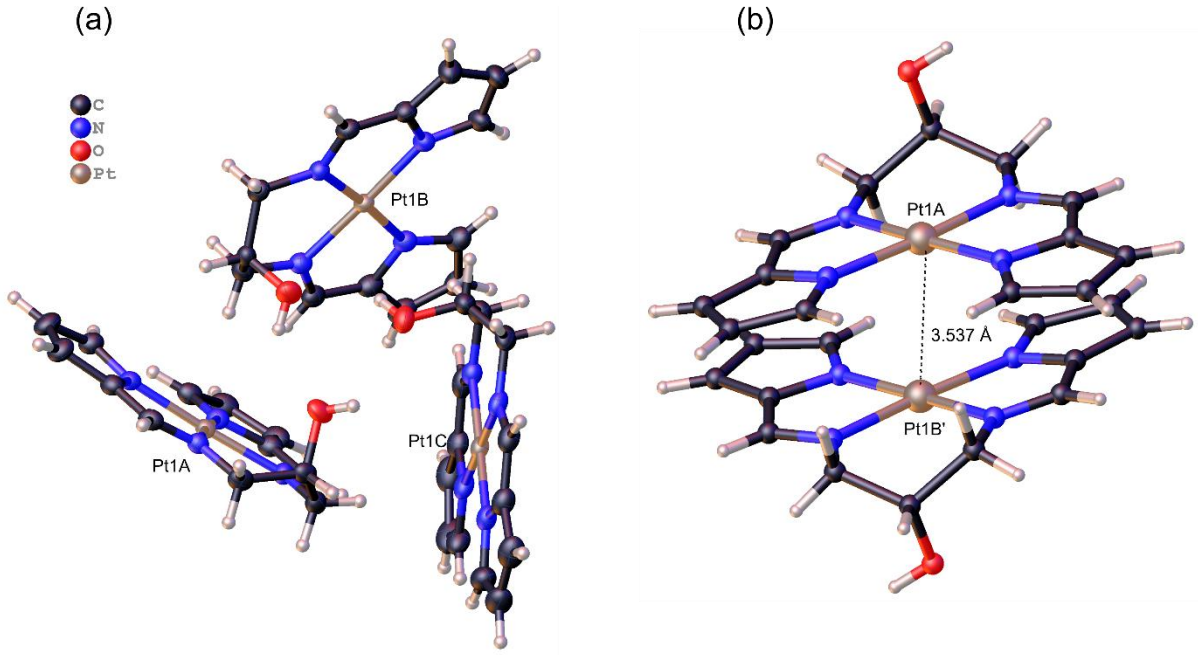

Fig. S12 (a) View of the ASU of complex **1**, which comprises three independent molecules supported by hydrogen bonding interactions between the hydroxyl groups of neighbouring molecules in the solid state. The hydroxyl groups act as both hydrogen bond donors and acceptors. (b) Intermolecular π-stacking arrangements of neighbouring molecules of **1** in adjacent ASUs. The Pt···Pt distances were measured between the pair of Pt(II) ions of a centrosymmetric inversion pair.

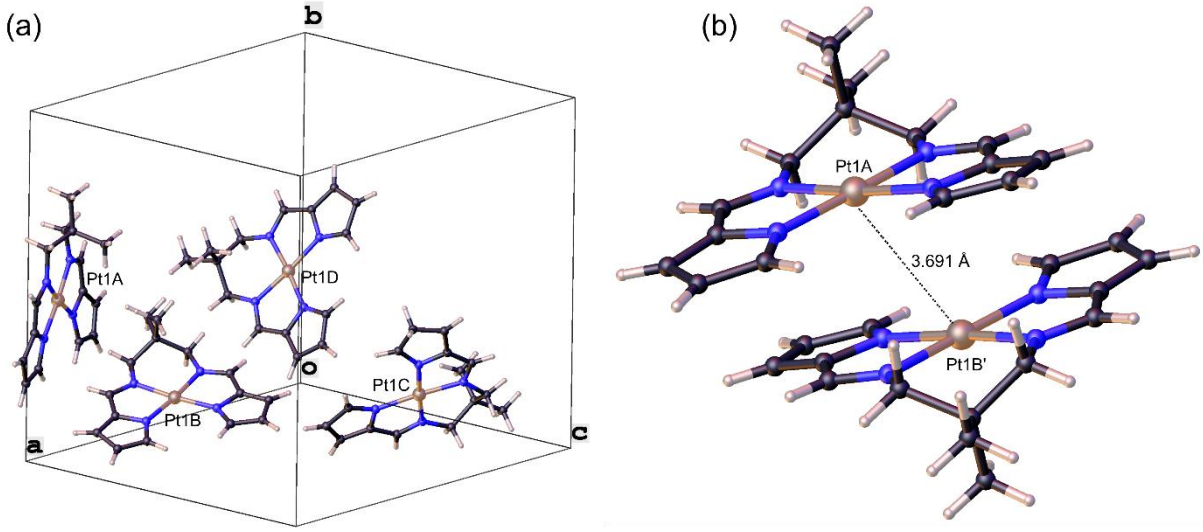

Fig. S13 (a) ASU of **2** comprising four independent molecules of **2** (b) Intermolecular π-stacking arrangements of neighbouring molecules of **2** in different ASUs. The Pt···Pt distances were measured between the pair of Pt(II) ions of a centrosymmetric inversion pair.

7.1.4. Fluorescence spectroscopy

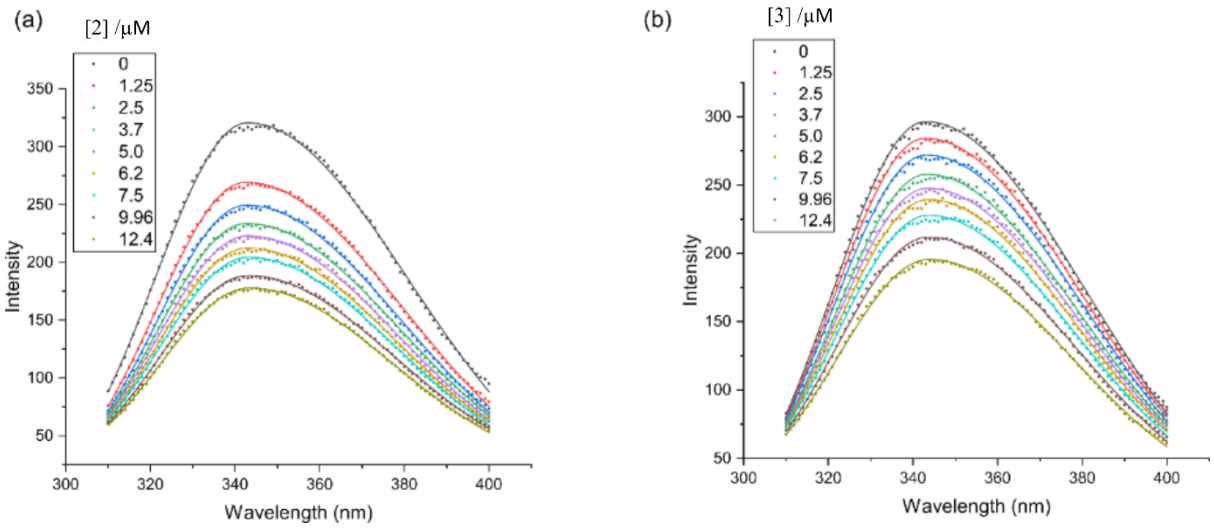

Fig. S14 Fluorescence emission spectra of HSA (5.0 μM) recorded as a function of increasing concentration of (a) **2** and (b) **3** at 298 K. Both Pt(II) bis(pyrrolide-imine) chelates had a concentration range of 0 – 12.4 μM. The emission spectra confirm that the Pt(II) complexes quench the intrinsic (i.e., Trp-214) fluorescence of HSA upon binding.

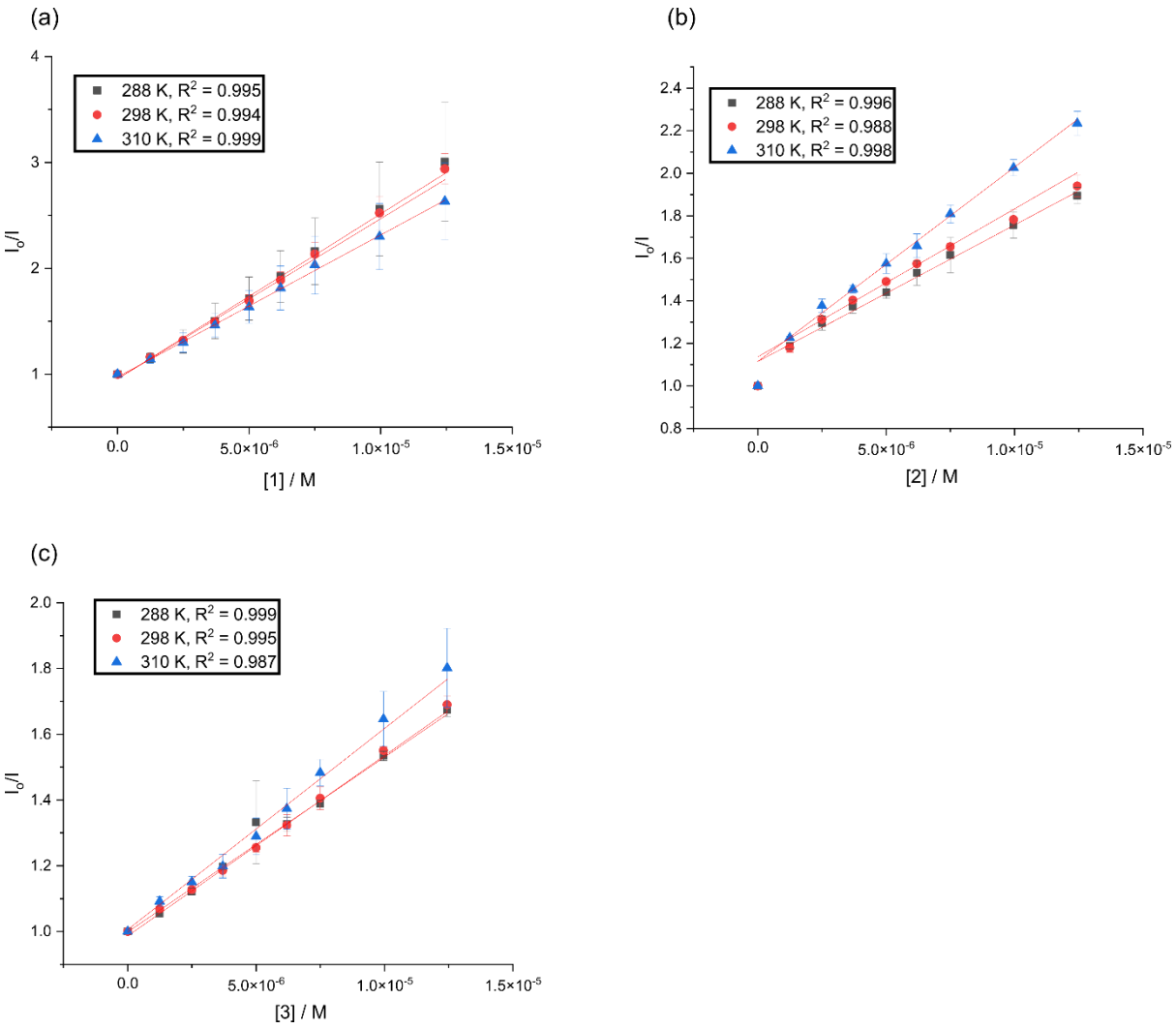

Fig. S15. Stern–Volmer plots of fluorescence quenching: (a) **1**···HSA, (b) **2**···HSA and (c) **3**···HSA. All three Pt(II) bis (pyrrolide-imine) chelates were recorded at three different temperatures (■ 288 K, ● 298 K, and ▲ 310 K). The relevant concentrations for the titrations were: [HSA] = 5.0 µM with **1**–**3** ranging from 0 – 12.4 µM at pH 7.50 in 50 mM KH_2PO_4 buffer.

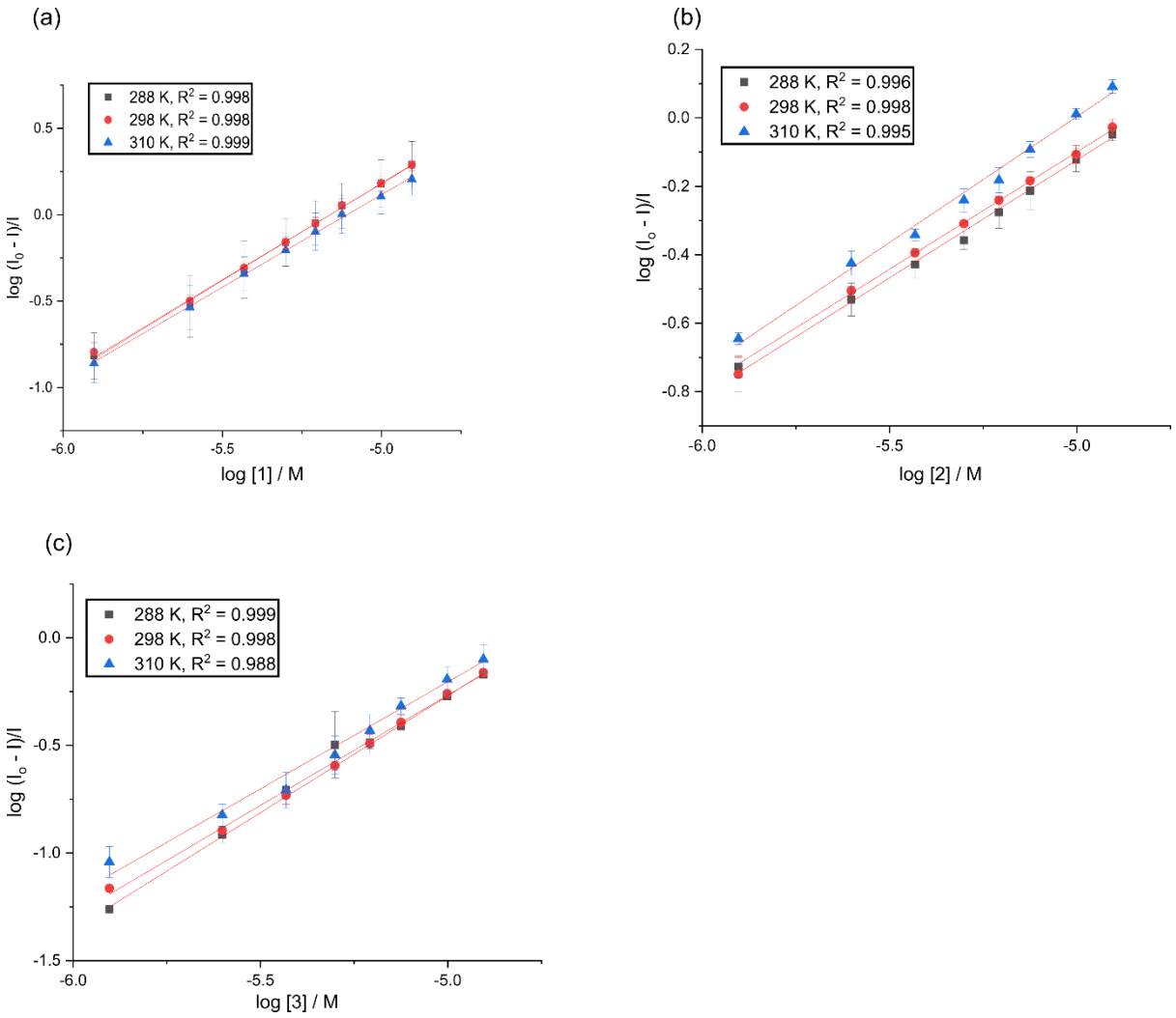

Fig. S16. Plots of $\log((I_0-I)/I)$ versus $\log([Q])$ for the interaction of HSA with several Pt(II) bis (pyrrolide-imine) chelates (i.e., quenchers, Q): (a) **1**···HSA complex, (b) **2**···HSA complex, and (c) **3**···HSA complex. The affinity constants are determined from the intercepts of the graphs and the stoichiometry from the slopes. Data for the three Pt(II) bis (pyrrolide-imine) chelates were recorded at three different temperatures (■ 288 K, ● 298 K, and ▲ 310 K). The relevant concentrations for the titrations were: [HSA] = 5.0 µM with **1**–**3** ranging from 0 – 12.4 µM at pH 7.50 in 50 mM KH_2PO_4 buffer.

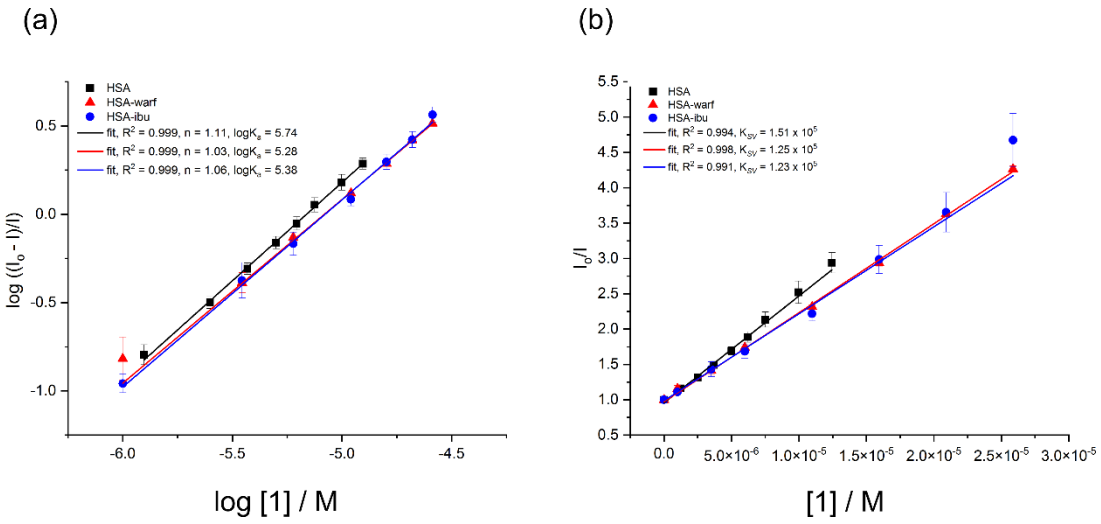

Fig. S17 (a) Double-log plot of the fluorescence quenching data, $log\left(\frac{I_0-I}{I}\right) = logK + nlog[Q]$, for native HSA, HSA•{warfarin}, and HSA•{Ibuprofen} as a function of the concentration of **1** at 298 K in KH_2PO_4 (50 mM, pH 7.50). This is to enable the measurement of logK_a (the association constant for the Pt(II) chelate with the macromolecule target, K_a) and the reaction stoichiometry (*n*). The excitation and emission wavelengths for the fluorophore probes were: (i) Trp-214 (native HSA), λ^{ex} = 295 nm, λ^{em} = 343 nm; (ii) Warfarin (HSA-Warf), λ^{ex} = 320 nm, λ^{em} = 382 nm, and (iii) Ibuprofen (HSA-Ibu), λ^{ex} = 228 nm, λ^{em} = 332 nm. (b) Stern–Volmer (SV) plot for native HSA, HSA•{warfarin}, and HSA•{Ibuprofen} as a function of the concentration of **1** at 298 K in KH_2PO_4 (50 mM, pH 7.50). The plots are linear with an intercept of 1.0 when static quenching is dominant. Overall, the plots show that **1** binds with an approximately 1:1 mole ratio to native HSA. The presence of either drug marginally decreases the binding of **1** as the affinity constants marginally decrease. A possible interpretation is that **1** can bind (half-saturate) to both subdomain IIA and IIIA (Sudlow's site I and II) of the native protein, but that when either warfarin or ibuprofen is located in one of these two sites, the reciprocal site is fully saturated. Alternatively, warfarin or ibuprofen may alter the protein conformation to enable the uptake of an additional half-equivalent of **1** at a third site. Such additional drug binding sites are known for HSA and exist in subdomains IIIB (propofol binding site, close to site II in subdomain IIIA) and IB (hemin binding site).

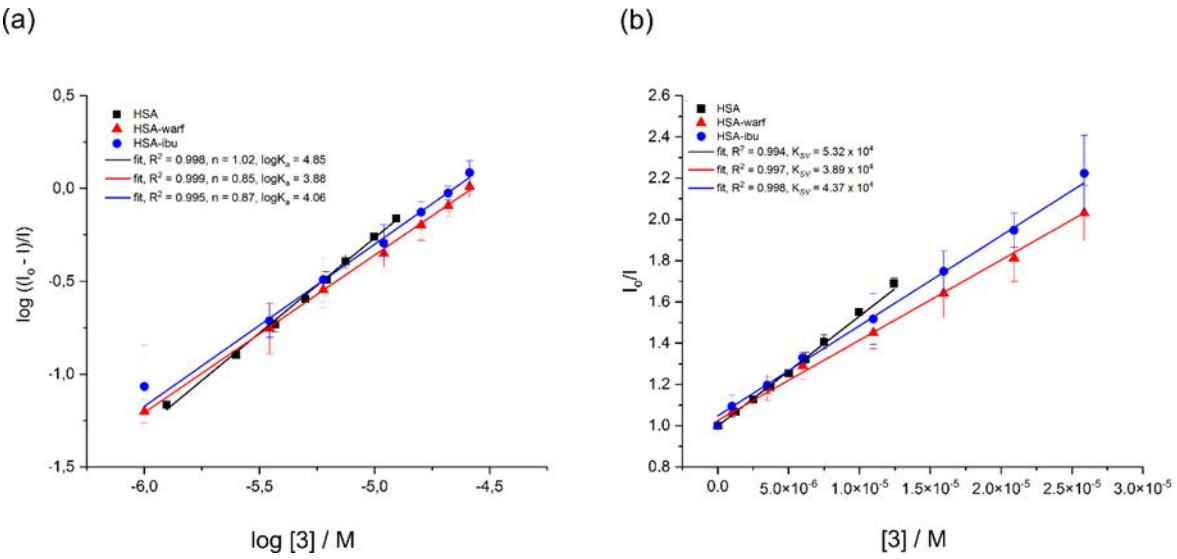

Fig. S18 (a) Double-log plot of the fluorescence quenching data, $log\left(\frac{I_0-I}{I}\right) = logK + nlog[Q]$, for native HSA, HSA•{warfarin}, and HSA•{Ibuprofen} as a function of the concentration of **3** at 298 K in KH_2PO_4 (50 mM, pH 7.50). This is to enable the measurement of logK_a (the association constant for the Pt(II) chelate with the macromolecule target, K_a) and the reaction stoichiometry (*n*). The excitation and emission wavelengths for the fluorophore probes were: (i) Trp-214 (native HSA), λ^{ex} = 295 nm, λ^{em} = 343 nm; (ii) Warfarin (HSA-Warf), λ^{ex} = 320 nm, λ^{em} = 382 nm, and (iii) Ibuprofen (HSA-Ibu), λ^{ex} = 228 nm, λ^{em} = 332 nm. (b) Stern–Volmer (SV) plot for native HSA, HSA•{warfarin}, and HSA•{Ibuprofen} as a function of the concentration of **3** at 298 K in KH_2PO_4 (50 mM, pH 7.50). The plots are linear with an intercept of 1.0 when static quenching is dominant. Overall, the plots show that **3** binds with an approximately 1:1 n value to native HSA. At no point does **3** displace either warfarin or ibuprofen from HSA•{warfarin}, and HSA•{Ibuprofen}; however, the presence of either drug marginally decreases the binding of **3** as the affinity constants marginally decrease. A possible interpretation is that **3** can bind (half-saturate) to both subdomain IIA and IIIA (Sudlow's site I and II) of the native protein, but that when either warfarin or ibuprofen is located in one of these two sites, the reciprocal site is fully saturated. Alternatively, warfarin or ibuprofen may alter the protein conformation to enable the uptake of an additional half-equivalent of **3** at a third site. Such additional drug binding sites are known for HSA and exist in subdomains IIIB (propofol binding site, close to site II in subdomain IIIA) and IB (hemin binding site).

7.1.5. CD spectroscopy

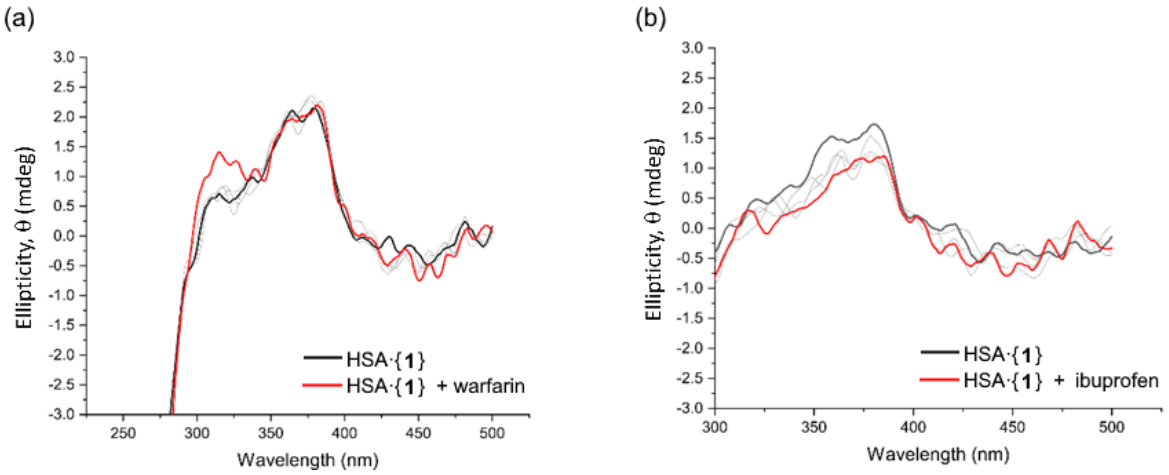

Fig. S19 Induced CD site displacement assay carried out by measuring the UV CD of HSA (15 µM in 50 mM KH_2PO_4 buffer, pH 7.5) bound to **1** (15 µM) from 280–500 nm. Site-specific markers (a) warfarin and (b) ibuprofen were titrated into the HSA•{**1**} solution to determine the Pt(II) chelate's preferred binding site. Both site-specific markers were titrated in to give concentrations of 4.1, 8.3, 12.5, and 20.1 µM (the grey lines represent 4.1, 8.3, and 12.5 µM). The spectra were smoothed using a Lowess function (0.07 span). From Fig. S19b, it is clear that only partial displacement of **1** is induced by the incoming probe ligand ibuprofen, while Fig. S19a indicates that incoming warfarin minimally perturbs the spectrum of HSA•{**1**} and evidently cannot displace **1** from the protein.

7.1.6. Molecular docking

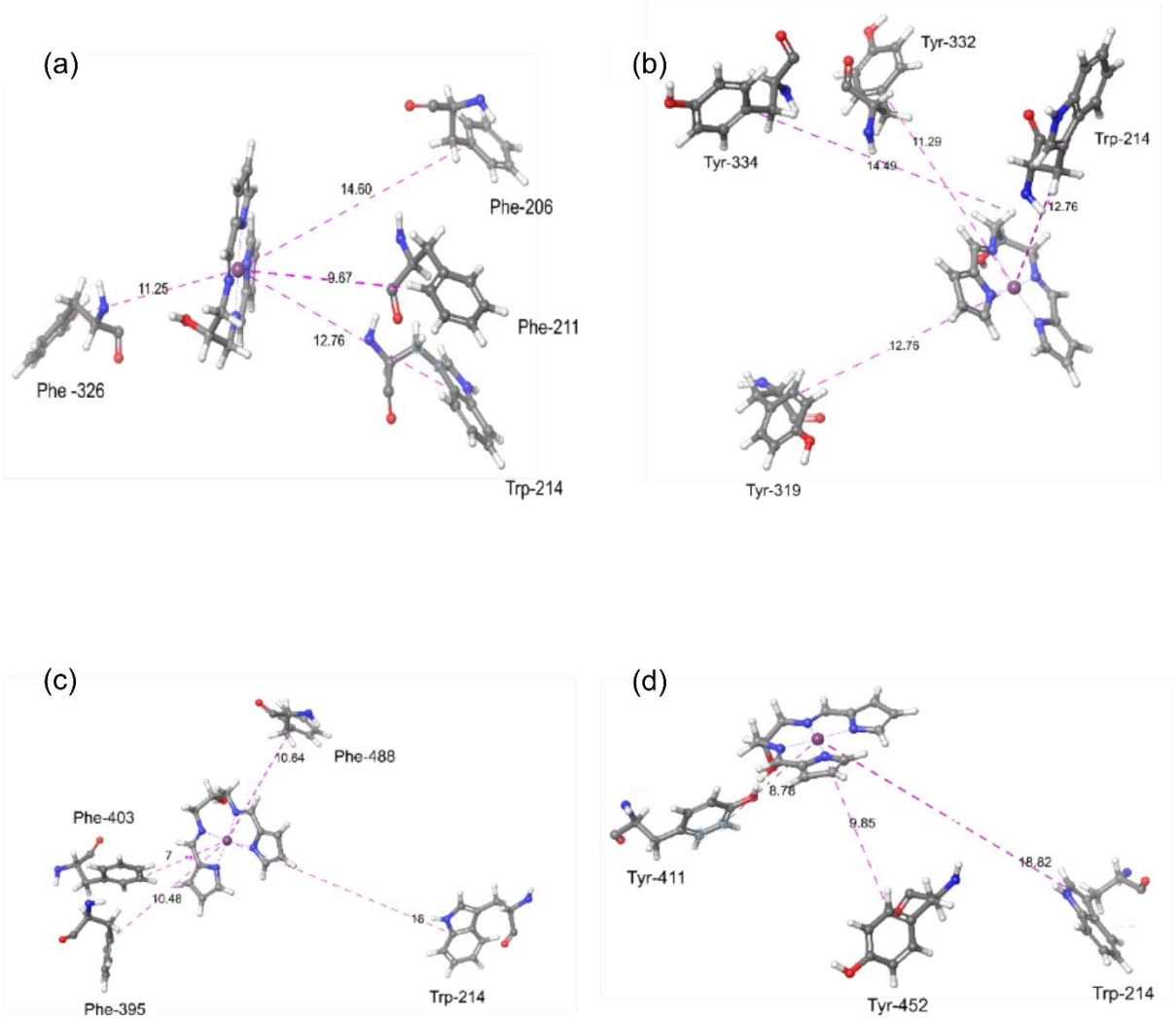

Fig. S20 GLIDE XP docking analysis of the binding of **1** to HSA using the X-ray structure of HSA as the *in silico* target (PDB code 1HA2). A large target grid was generated for macromolecular ligand docking at the warfarin site (with warfarin removed), spanning 40 x 40 x 40 Å^3, to search for secondary binding sites radiating out (to ~20 Å) from warfarin's location in subdomain IIA. The image panels show selected phenylaniline and tyrosine residues, respectively, that are closest to the best poses for **1** (a summary of the aromatic residues for **2** is given in Table S8). Distances are in Å units. The near-UV CD spectra for HSA•{**1**} and HSA•{**2**} are shown in Figs. 7a and b of in the main text suggest that these ligands perturb Tyr and Phe chromophores in addition to Trp-214 in HSA. The above docking results support the experimental data: **2** binds in tyrosine- and phenylalanine-rich pockets within HSA with roughly the same docking score.

(a)

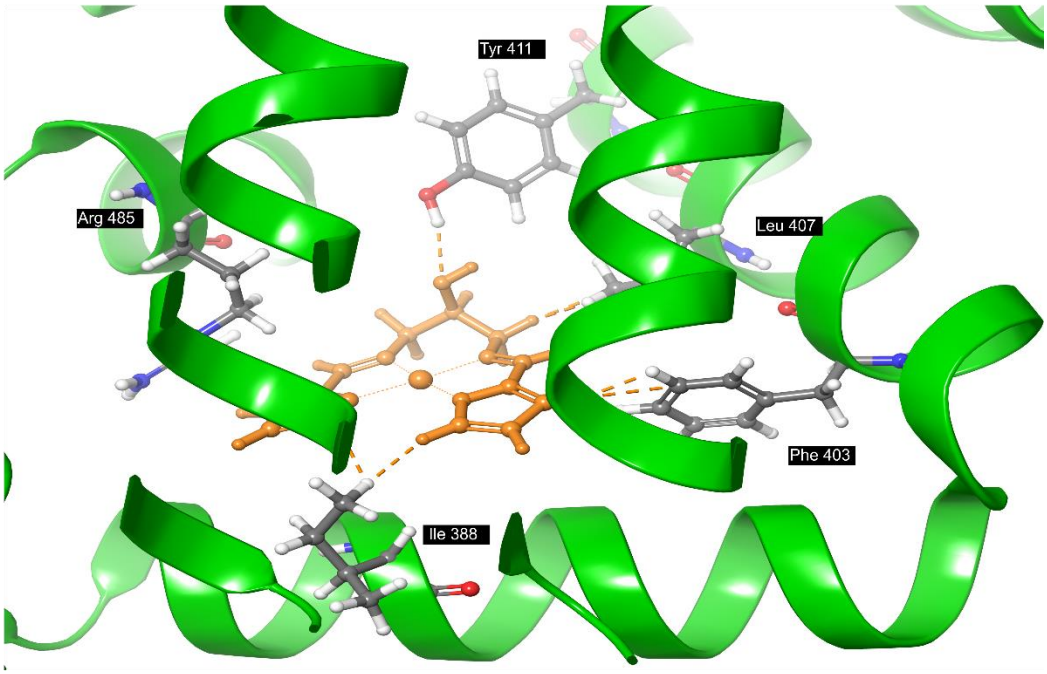

(b)

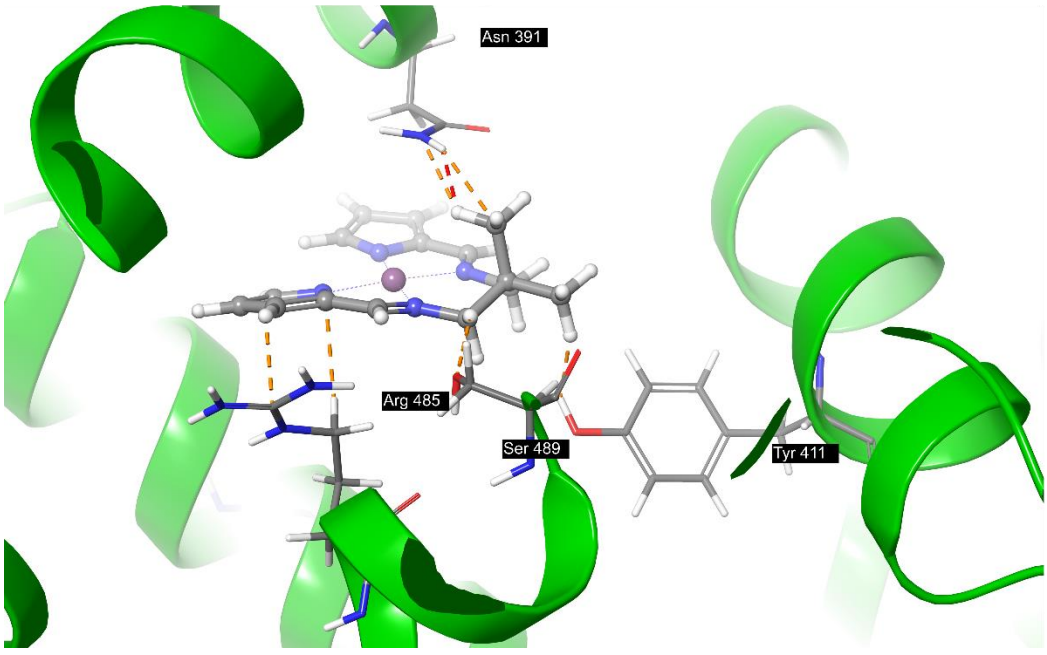

Fig. S21 Illustration of the binding of Pt(II) chelates **1** and **2** in subdomain IIIA (Sudlow's drug site II) of HSA as determined by GLIDE XP docking using PDB code 2BXF as the target and a large 40 × 40 × 40-Å^3 grid centred on the coordinates of diazepam. The *in silico* model supports the observed data suggesting both Pt(II) chelates **1** and **2** bind to Sudlow's site II (See Figs. 7 and 9 of the main paper.)

7.1.7. Solution stability tests

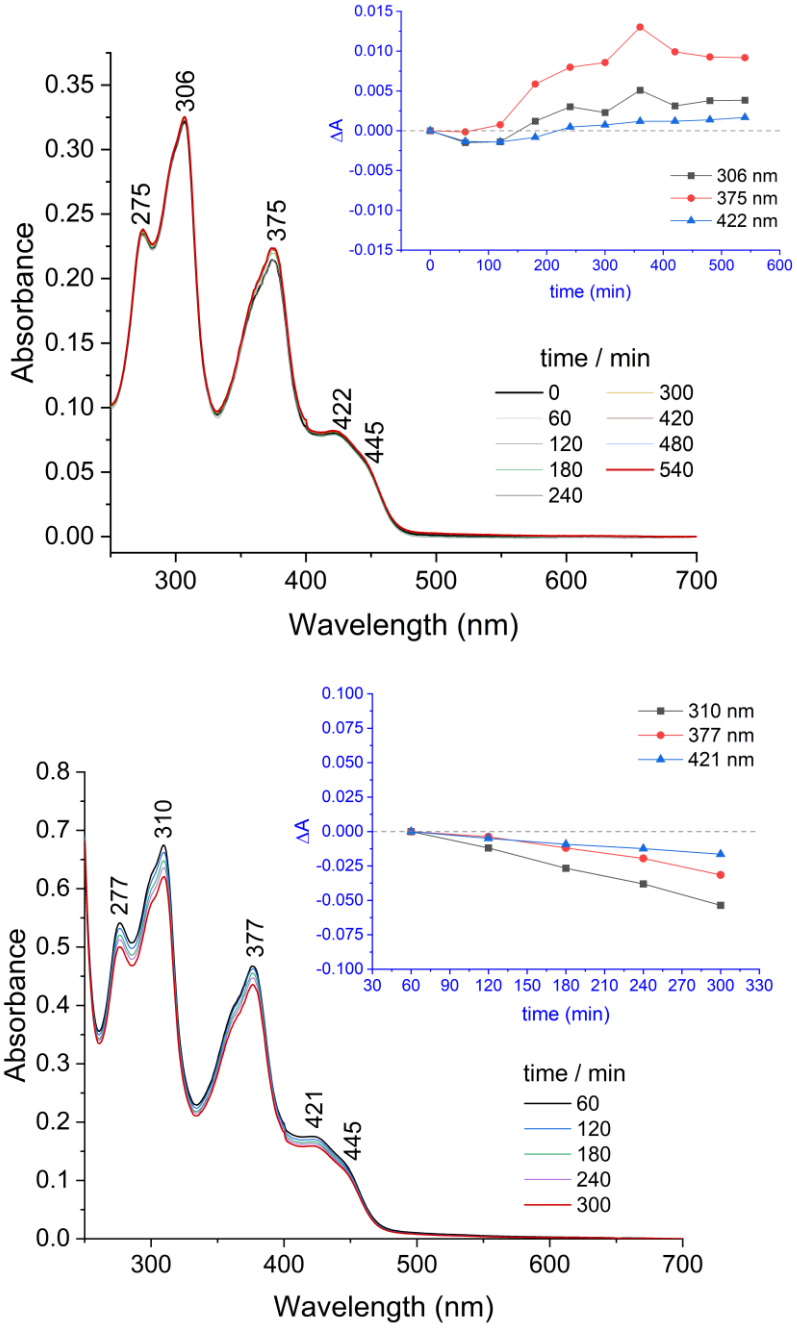

Fig. S22 UV-vis spectra of 20-µM solutions of **1** (top) and **2** (bottom) recorded as a function of time in KH_2PO_4 buffer (50 mM pH 7.5). The solution of Pt(II) complex **1** had DMSO < 1% (V/V), while the solution of **2** had a final DMSO content of 20% (V/V). As shown by the inset plot for the spectra of **1**, the absorption maxima change negligibly with time. There are also no isosbestic points in the spectra. The data indicate that the complex undergoes no chemical reactions over the time interval investigated, with instrumental drift and slight solution evaporation accounting for the subtle absorbance changes. For complex **2**, the slightly more pronounced monotonic decrease in band intensity with time, without accompanying isosbestic points or band broadening, suggests gradual, partial precipitation of the compound. This observation reflects the more nonpolar structure of **2** compared with **1**. (Precipitation was even more prevalent for **3**; Fig. S23.)

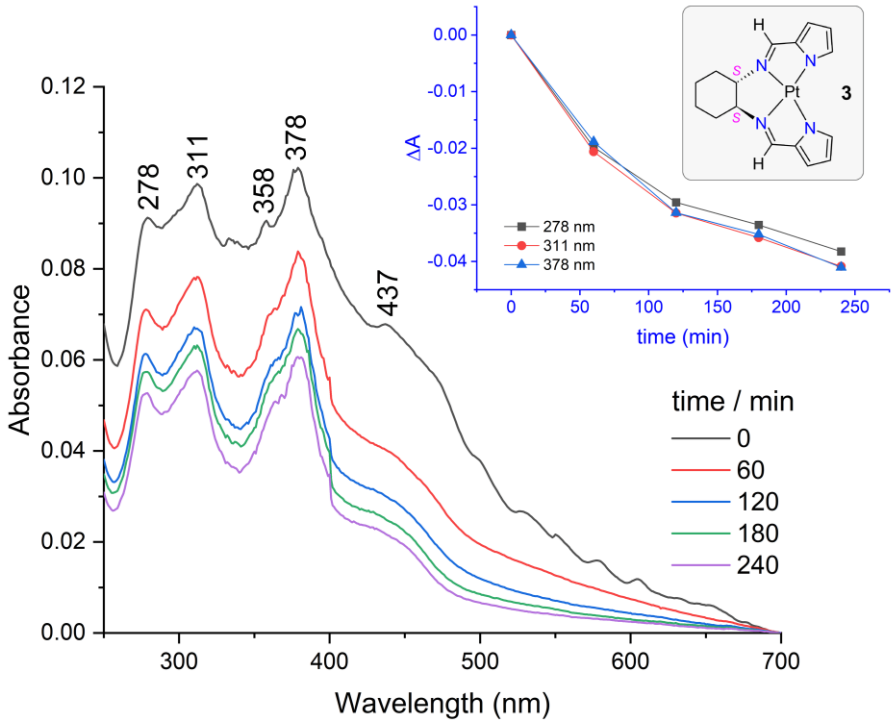

Fig. S23 UV-vis spectra of a 20 µM solution of **3** recorded as a function of time in KH_2PO_4 buffer (50 mM pH 7.5, 20% DMSO (V/V)). The poor solubility of the complex is evident from the low intensity of the spectra, their higher noise relative to spectra of **1** and **2** at the same concentration, and the monotonic decrease in intensity with time over the full wavelength range. The kinetic data reflect precipitation of the complex, which is earmarked by the lack of isosbestic points accompanying the spectral changes. The initial spectrum at t = 0 min is especially broad and shows multiple band maxima, suggesting that the complex is significantly aggregated despite the DMSO content being 20% (V/V). Importantly, the spectral band maxima at $t \geq 60$ min only change in intensity and do not undergo wavelength shifts. This indicates that no chemical reaction is occurring, such as complex hydrolysis or demetallation. From our TD-DFT assignments of the band maxima, loss of the Pt(II) ion from the chelate would eliminate the peak at 311 nm in the spectrum because this is an almost pure (97%) metal-to-ligand (MLCT) transition (Pt $5dz^2 \rightarrow$ p*,π*). Moreover, all bands > 350 nm may be ascribed to transitions involving ligand molecular orbitals (MOs) that are heavily mixed with Pt 5dxz and 5dyz atomic orbitals; demetallation would thus significantly affect the electronic spectra of **1**–**3** in this region of the spectrum. Finally, at no point does the spectrum of the free ligand begin to appear in the spectra. The Pt(II) chelates studied here are thus chemically stable under the conditions employed for the protein binding experiments, which leads to the uptake of fully intact metal complexes.

7.1.8. Solvent effects for TD-DFT calculated UV-vis spectra

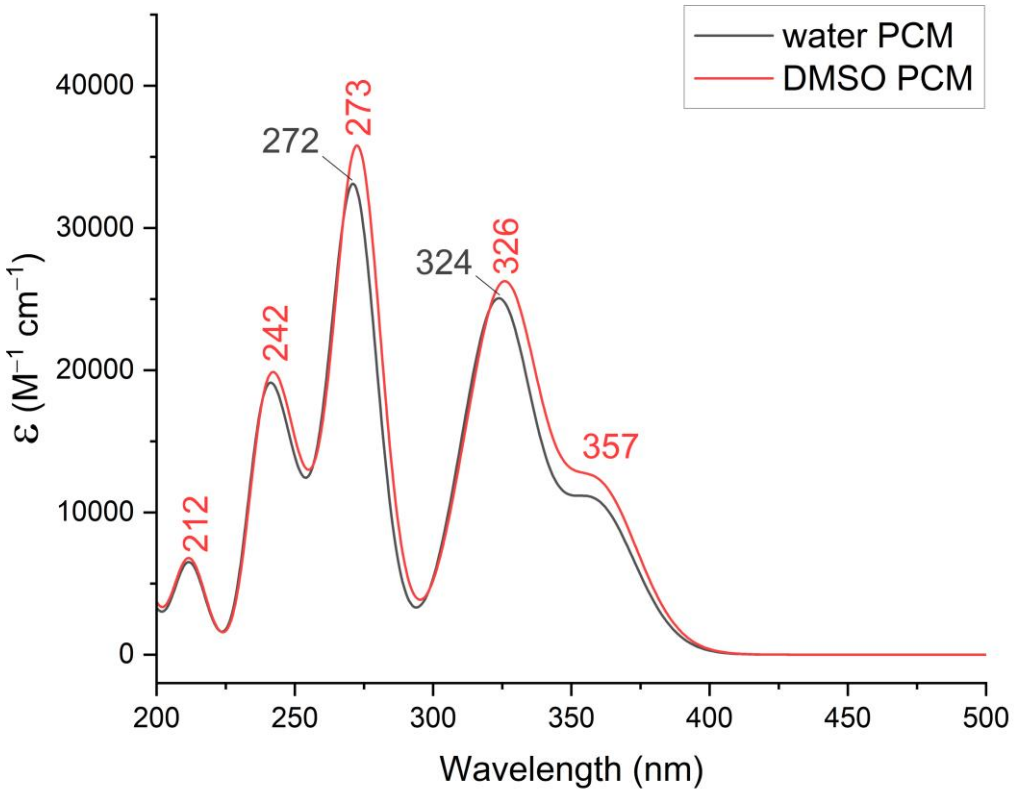

Fig. S24 Electronic spectra of **1** calculated by the TD-DFT method (CAM-B3LYP/def2-QZVP/GD3BJ level of theory) in water and DMSO (PCM solvent continua). The spectra are similar for the two solvent systems with band maxima differing by at most 2 nm for bands > 300 nm. The overall shape and intensity profile of the bands is similar with longer-wavelength bands exhibiting a somewhat higher intensity in DMSO (8% at 273 nm). The band width for calculation of the spectral envelope in each case was 2500 Hz (fwhm).

8. Tables

Table S1. Crystal data and X-ray structure refinement details for Pt(II) bis(pyrrolide-imine) chelates **1** and **2**.

Empirical formula	$C_{13}H_{14}N_4OPt$ (**1**)	$C_{15}H_{18}N_4Pt$ (**2**)
CCDC deposit number	**2271559**	**2271558**
Formula weight	437.37	449.42
Temperature/K	173(2)	173(2)
Crystal system	triclinic	triclinic
Space group	*P*-1	*P*-1
a/Å	9.0752(19)	13.7803(5)
b/Å	12.639(3)	15.2877(5)
c/Å	18.870(3)	16.8165(6)
α/°	108.653(7)	103.788(2)
β/°	90.856(8)	104.926(2)
γ/°	96.322(9)	107.795(2)
Volume/Å^3	2035.3(7)	3059.76(19)
Z	6	8
Pcalc g/cm^3	2.141	1.951
μ/mm^{-1}	10.338	9.167
F(000)	1236.0	1712.0
Crystal size/mm^3	0.180 × 0.050 × 0.050	0.227 × 0.161 × 0.076
Radiation	MoKα (λ = 0.71073 Å)	MoKα (λ = 0.71073 Å)
Index ranges	-13 ≤ h ≤ 13, -19 ≤ k ≤ 19, -29 ≤ l ≤ 29	-19 ≤ h ≤ 19, -21 ≤ k ≤ 21, -24 ≤ l ≤ 24
Reflections collected	139345	113600
Independent reflections	15567 [R_{int} = 0.0636, R_{sigma} = 0.0358]	18723 [R_{int} = 0.0665, R_{sigma} = 0.0536]
Data/restraints/parameters	15567/0/514	18723/0/729
Goodness-of-fit on F^2	1.050	1.004
Final R indexes [I>=2σ (I)]	R_1 = 0.0308, wR_2 = 0.0643	R_1 = 0.0327, wR_2 = 0.0527
Final R indexes [all data]	R_1 = 0.0444, wR_2 = 0.0689	R_1 = 0.0586, wR_2 = 0.0590
Largest diff. peak/hole / e Å^{-3}	1.90/-1.46	0.96/-1.10
Disordered solvent mask	1 void/cell, 98 electrons, V = 172 Å^3, 1.5 H_2O/ASU	3 voids/cell, 27 electrons, V = 229 Å^3, 1.2 H_2O/ASU

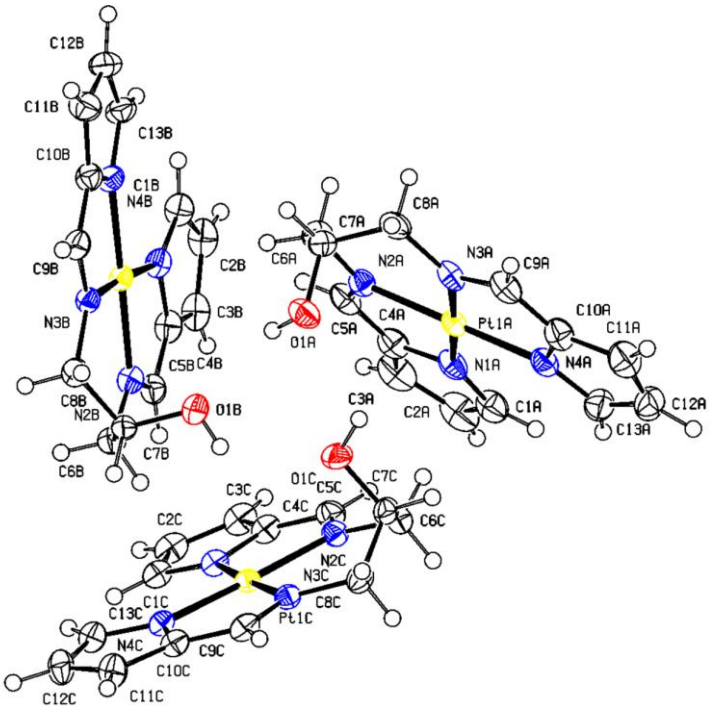

Table S2. Selected geometrical parameters (Å, °) for the X-ray structure of **1** and **2**. A labelled thermal ellipsoid plot (50% probability surfaces) is included above to aid in reading the tabulated data.

Atom		Length/Å	Atom		Length/Å
Pt1C	N3C	2.009(3)	N2A	C5A	1.290(5)
Pt1C	N2C	2.009(3)	N2A	C6A	1.452(6)
Pt1C	N4C	2.012(3)	N1B	C1B	1.354(5)
Pt1C	N1C	2.017(3)	N1B	C4B	1.386(5)
Pt1B	N2B	2.003(3)	C5A	C4A	1.420(7)
Pt1B	N3B	2.004(3)	C9C	C10C	1.423(6)
Pt1B	N4B	2.011(3)	C3A	C2A	1.384(8)
Pt1B	N1B	2.017(3)	C3A	C4A	1.409(6)
Pt1A	N2A	2.000(3)	C4C	C3C	1.389(6)
Pt1A	N1A	2.008(4)	C4C	C5C	1.420(6)
Pt1A	N3A	2.009(3)	C2B	C3B	1.399(7)
Pt1A	N4A	2.014(4)	C2B	C1B	1.407(6)
O1B	C7B	1.413(5)	C9A	C10A	1.425(7)
O1C	C7C	1.410(5)	C10C	C11C	1.395(6)
N3A	C9A	1.292(6)	C9B	C10B	1.419(6)
N3A	C8A	1.464(6)	C8B	C7B	1.518(6)
O1A	C7A	1.428(5)	C4B	C3B	1.397(6)
N1C	C1C	1.356(5)	C4B	C5B	1.423(6)
N1C	C4C	1.388(5)	C7B	C6B	1.523(6)
N2C	C5C	1.304(5)	C3C	C2C	1.405(7)
N2C	C6C	1.465(5)	C2C	C1C	1.392(6)
N4C	C13C	1.345(5)	C2A	C1A	1.386(7)
N4C	C10C	1.386(5)	C10A	C11A	1.398(7)
N3C	C9C	1.294(5)	C8A	C7A	1.525(6)

N3C	C8C	1.456(5)	C8C	C7C	1.523(6)
N4A	C13A	1.345(6)	C12B	C11B	1.385(6)
N4A	C10A	1.373(6)	C12B	C13B	1.404(7)
N4B	C13B	1.352(5)	C10B	C11B	1.397(6)
N4B	C10B	1.382(5)	C11A	C12A	1.387(8)
N3B	C9B	1.306(5)	C11C	C12C	1.393(6)
N3B	C8B	1.467(5)	C7C	C6C	1.521(6)
N2B	C5B	1.304(5)	C12C	C13C	1.392(6)
N2B	C6B	1.460(5)	C12A	C13A	1.404(7)
N1A	C1A	1.358(6)	C6A	C7A	1.517(6)
N1A	C4A	1.393(6)			

Atom			Angle/°	Atom			Angle/°
N3C	Pt1C	N2C	95.58(14)	C2A	C3A	C4A	105.9(4)
N3C	Pt1C	N4C	80.47(13)	N1C	C4C	C3C	109.9(4)
N2C	Pt1C	N4C	174.81(13)	N1C	C4C	C5C	114.7(3)
N3C	Pt1C	N1C	175.57(13)	C3C	C4C	C5C	135.5(4)
N2C	Pt1C	N1C	80.13(14)	C3B	C2B	C1B	107.0(4)
N4C	Pt1C	N1C	103.88(13)	N2C	C5C	C4C	116.9(4)
N2B	Pt1B	N3B	95.66(13)	N3A	C9A	C10A	117.6(4)
N2B	Pt1B	N4B	175.79(13)	N4C	C10C	C11C	109.6(4)
N3B	Pt1B	N4B	80.19(13)	N4C	C10C	C9C	114.8(3)
N2B	Pt1B	N1B	80.38(14)	C11C	C10C	C9C	135.5(4)
N3B	Pt1B	N1B	175.65(13)	N3B	C9B	C10B	116.5(4)
N4B	Pt1B	N1B	103.74(14)	N3B	C8B	C7B	113.3(3)
N2A	Pt1A	N1A	80.27(15)	N1B	C4B	C3B	109.1(4)
N2A	Pt1A	N3A	95.70(15)	N1B	C4B	C5B	114.8(4)
N1A	Pt1A	N3A	175.50(15)	C3B	C4B	C5B	136.0(4)
N2A	Pt1A	N4A	175.66(14)	O1B	C7B	C8B	108.6(3)
N1A	Pt1A	N4A	103.89(16)	O1B	C7B	C6B	113.2(3)
N3A	Pt1A	N4A	80.19(15)	C8B	C7B	C6B	114.5(3)
C9A	N3A	C8A	121.3(4)	N2B	C5B	C4B	116.8(4)
C9A	N3A	Pt1A	114.7(3)	C4C	C3C	C2C	105.7(4)
C8A	N3A	Pt1A	123.8(3)	C1C	C2C	C3C	107.9(4)
C1C	N1C	C4C	107.2(3)	C3A	C2A	C1A	108.0(4)
C1C	N1C	Pt1C	139.8(3)	C4B	C3B	C2B	106.7(4)
C4C	N1C	Pt1C	113.0(3)	N4A	C10A	C11A	110.7(4)
C5C	N2C	C6C	120.8(3)	N4A	C10A	C9A	114.3(4)

C5C	N2C	Pt1C	115.4(3)	C11A	C10A	C9A	135.0(5)
C6C	N2C	Pt1C	123.8(3)	N1A	C4A	C3A	109.5(4)
C13C	N4C	C10C	106.9(3)	N1A	C4A	C5A	114.4(4)
C13C	N4C	Pt1C	140.5(3)	C3A	C4A	C5A	136.2(5)
C10C	N4C	Pt1C	112.5(3)	N3A	C8A	C7A	113.1(3)
C9C	N3C	C8C	121.2(3)	N1C	C1C	C2C	109.3(4)
C9C	N3C	Pt1C	115.0(3)	N3C	C8C	C7C	112.1(3)
C8C	N3C	Pt1C	123.9(3)	C11B	C12B	C13B	107.3(4)
C13A	N4A	C10A	107.4(4)	N4B	C10B	C11B	109.4(4)
C13A	N4A	Pt1A	139.4(3)	N4B	C10B	C9B	114.9(4)
C10A	N4A	Pt1A	113.0(3)	C11B	C10B	C9B	135.7(4)
C13B	N4B	C10B	107.3(3)	C12B	C11B	C10B	106.6(4)
C13B	N4B	Pt1B	139.7(3)	N1A	C1A	C2A	110.3(5)
C10B	N4B	Pt1B	113.0(3)	C12A	C11A	C10A	104.5(5)
C9B	N3B	C8B	120.9(3)	C12C	C11C	C10C	106.0(4)
C9B	N3B	Pt1B	115.4(3)	O1C	C7C	C6C	112.7(3)
C8B	N3B	Pt1B	123.8(3)	O1C	C7C	C8C	107.9(3)
C5B	N2B	C6B	120.4(4)	C6C	C7C	C8C	114.0(3)
C5B	N2B	Pt1B	115.3(3)	N2B	C6B	C7B	113.0(3)
C6B	N2B	Pt1B	124.3(3)	N2C	C6C	C7C	113.6(3)
C1A	N1A	C4A	106.2(4)	C13C	C12C	C11C	107.5(4)
C1A	N1A	Pt1A	141.0(3)	C11A	C12A	C13A	108.8(5)
C4A	N1A	Pt1A	112.7(3)	N1B	C1B	C2B	109.4(4)
C5A	N2A	C6A	120.1(4)	N4C	C13C	C12C	110.1(4)
C5A	N2A	Pt1A	115.6(3)	N4B	C13B	C12B	109.5(4)
C6A	N2A	Pt1A	124.1(3)	N2A	C6A	C7A	115.2(4)
C1B	N1B	C4B	107.7(3)	N4A	C13A	C12A	108.6(5)
C1B	N1B	Pt1B	139.5(3)	O1A	C7A	C6A	112.9(4)
C4B	N1B	Pt1B	112.7(3)	O1A	C7A	C8A	107.2(4)
N2A	C5A	C4A	117.0(4)	C6A	C7A	C8A	114.5(4)
N3C	C9C	C10C	117.2(3)				

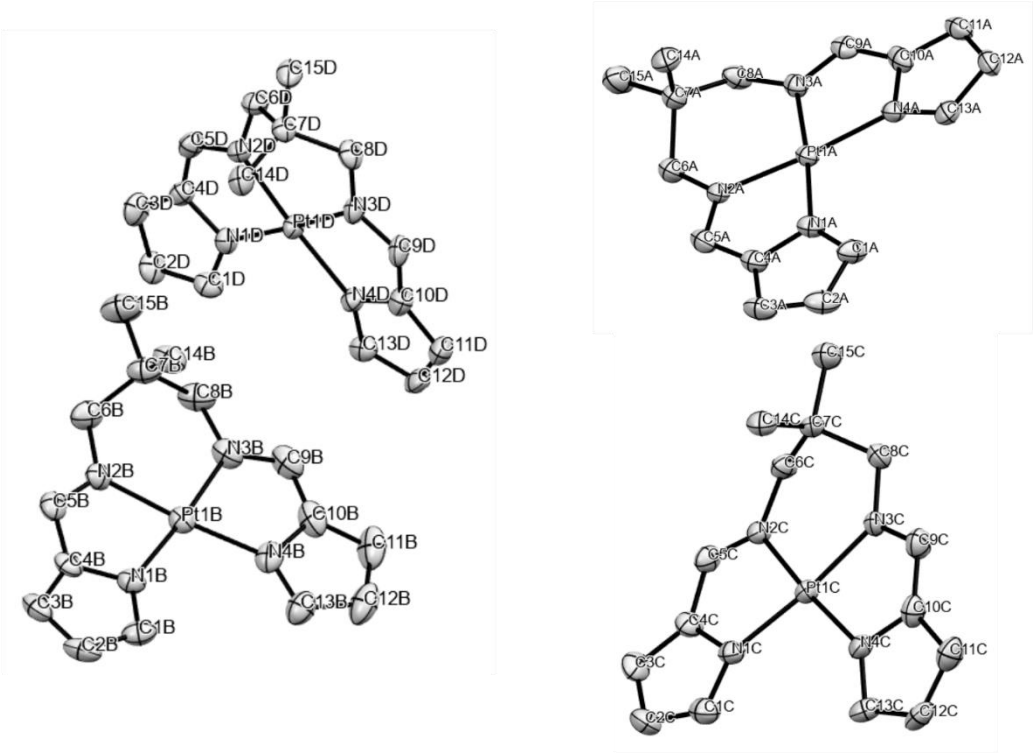

Table S3. Selected geometrical parameters (Å, °) for the X-ray structure of **1** and **2**. A labelled thermal ellipsoid plot (50% probability surfaces, H atoms omitted for clarity) is included above to aid in reading the tabulated data.

Atom	Length/Å	Atom	Length/Å
Pt1A N1A	2.016(3)	Pt1C N1C	2.013(3)
Pt1A N2A	2.005(3)	Pt1C N2C	2.003(3)
Pt1A N3A	2.003(3)	Pt1C N3C	2.001(3)
Pt1A N4A	2.010(3)	Pt1C N4C	2.015(3)
N1A C1A	1.344(5)	N1C C1C	1.344(5)
N1A C4A	1.377(5)	N1C C4C	1.375(5)
N2A C5A	1.304(5)	N2C C5C	1.293(5)
N2A C6A	1.467(5)	N2C C6C	1.460(5)
N3A C8A	1.466(5)	N3C C8C	1.470(5)
N3A C9A	1.298(5)	N3C C9C	1.300(5)
N4A C10A	1.383(5)	N4C C10C	1.387(5)
N4A C13A	1.343(5)	N4C C13C	1.352(5)
C1A C2A	1.390(6)	C1C C2C	1.390(6)
C2A C3A	1.388(6)	C2C C3C	1.391(6)
C3A C4A	1.396(5)	C3C C4C	1.380(6)
C4A C5A	1.435(6)	C4C C5C	1.421(6)
C6A C7A	1.536(5)	C6C C7C	1.539(5)
C7A C8A	1.531(6)	C7C C8C	1.535(5)
C7A C14A	1.528(6)	C7C C14C	1.516(6)
C7A C15A	1.534(6)	C7C C15C	1.535(5)

Atom		Length/Å	Atom		Length/Å
C9A	C10A	1.416(6)	C9C	C10C	1.417(6)
C10A	C11A	1.384(6)	C10C	C11C	1.398(6)
C11A	C12A	1.398(6)	C11C	C12C	1.381(6)
C12A	C13A	1.389(6)	C12C	C13C	1.387(6)
Pt1B	N1B	2.013(3)	Pt1D	N1D	2.010(3)
Pt1B	N2B	2.000(3)	Pt1D	N2D	2.000(3)
Pt1B	N3B	1.996(4)	Pt1D	N3D	2.009(3)
Pt1B	N4B	2.012(4)	Pt1D	N4D	2.012(3)
N1B	C1B	1.340(5)	N1D	C1D	1.336(5)
N1B	C4B	1.383(5)	N1D	C4D	1.375(5)
N2B	C5B	1.295(5)	N2D	C5D	1.304(5)
N2B	C6B	1.470(5)	N2D	C6D	1.460(5)
N3B	C8B	1.467(6)	N3D	C8D	1.467(5)
N3B	C9B	1.296(6)	N3D	C9D	1.291(5)
N4B	C10B	1.388(6)	N4D	C10D	1.385(5)
N4B	C13B	1.351(6)	N4D	C13D	1.354(5)
C1B	C2B	1.388(6)	C1D	C2D	1.391(6)
C2B	C3B	1.369(6)	C2D	C3D	1.391(6)
C3B	C4B	1.398(6)	C3D	C4D	1.389(6)
C4B	C5B	1.421(6)	C4D	C5D	1.414(6)
C6B	C7B	1.545(6)	C6D	C7D	1.544(5)
C7B	C8B	1.539(6)	C7D	C8D	1.534(5)
C7B	C14B	1.522(6)	C7D	C14D	1.523(5)
C7B	C15B	1.526(6)	C7D	C15D	1.528(5)
C9B	C10B	1.411(7)	C9D	C10D	1.421(6)
C10B	C11B	1.402(7)	C10D	C11D	1.382(6)
C11B	C12B	1.378(7)	C11D	C12D	1.385(6)
C12B	C13B	1.394(6)	C12D	C13D	1.392(6)

Atom	Atom	Atom	Angle/˚	Atom	Atom	Atom	Angle/˚
N2A	Pt1A	N1A	80.20(13)	N1C	Pt1C	N4C	104.34(13)
N2A	Pt1A	N4A	175.22(13)	N2C	Pt1C	N1C	79.76(13)
N3A	Pt1A	N1A	175.41(14)	N2C	Pt1C	N4C	175.67(13)
N3A	Pt1A	N2A	95.63(13)	N3C	Pt1C	N1C	174.26(13)
N3A	Pt1A	N4A	79.95(13)	N3C	Pt1C	N2C	95.77(13)
N4A	Pt1A	N1A	104.15(13)	N3C	Pt1C	N4C	80.22(13)
C1A	N1A	Pt1A	140.1(3)	C1C	N1C	Pt1C	138.8(3)
C1A	N1A	C4A	107.0(3)	C1C	N1C	C4C	107.1(4)
C4A	N1A	Pt1A	112.9(3)	C4C	N1C	Pt1C	113.5(3)
C5A	N2A	Pt1A	115.9(3)	C5C	N2C	Pt1C	115.4(3)
C5A	N2A	C6A	120.6(3)	C5C	N2C	C6C	122.3(3)
C6A	N2A	Pt1A	123.5(2)	C6C	N2C	Pt1C	122.1(2)

Atom	Atom	Atom	Angle/˚	Atom	Atom	Atom	Angle/˚
C8A	N3A	Pt1A	123.8(2)	C8C	N3C	Pt1C	124.1(2)
C9A	N3A	Pt1A	115.4(3)	C9C	N3C	Pt1C	115.5(3)
C9A	N3A	C8A	120.9(3)	C9C	N3C	C8C	120.3(3)
C10A	N4A	Pt1A	113.3(3)	C10C	N4C	Pt1C	112.6(3)
C13A	N4A	Pt1A	140.3(3)	C13C	N4C	Pt1C	140.1(3)
C13A	N4A	C10A	106.2(3)	C13C	N4C	C10C	107.1(3)
N1A	C1A	C2A	110.0(4)	N1C	C1C	C2C	109.8(4)
C3A	C2A	C1A	107.4(4)	C1C	C2C	C3C	107.0(4)
C2A	C3A	C4A	105.9(4)	C4C	C3C	C2C	106.5(4)
N1A	C4A	C3A	109.6(4)	N1C	C4C	C3C	109.7(4)
N1A	C4A	C5A	115.2(3)	N1C	C4C	C5C	114.0(4)
C3A	C4A	C5A	135.1(4)	C3C	C4C	C5C	136.1(4)
N2A	C5A	C4A	115.8(4)	N2C	C5C	C4C	117.2(4)
N2A	C6A	C7A	113.6(3)	N2C	C6C	C7C	113.7(3)
C8A	C7A	C6A	111.6(3)	C8C	C7C	C6C	110.2(3)
C8A	C7A	C15A	106.3(4)	C14C	C7C	C6C	111.1(3)
C14A	C7A	C6A	110.6(4)	C14C	C7C	C8C	112.2(3)
C14A	C7A	C8A	110.9(3)	C14C	C7C	C15C	109.8(3)
C14A	C7A	C15A	109.8(4)	C15C	C7C	C6C	106.9(3)
C15A	C7A	C6A	107.3(3)	C15C	C7C	C8C	106.4(3)
N3A	C8A	C7A	114.5(3)	N3C	C8C	C7C	114.5(3)
N3A	C9A	C10A	117.2(4)	N3C	C9C	C10C	116.8(4)
N4A	C10A	C9A	114.2(4)	N4C	C10C	C9C	114.8(4)
N4A	C10A	C11A	110.3(4)	N4C	C10C	C11C	108.6(4)
C11A	C10A	C9A	135.3(4)	C11C	C10C	C9C	136.5(4)
C10A	C11A	C12A	106.0(4)	C12C	C11C	C10C	107.0(4)
C13A	C12A	C11A	106.8(4)	C11C	C12C	C13C	107.3(4)
N4A	C13A	C12A	110.8(4)	N4C	C13C	C12C	110.0(4)
N2B	Pt1B	N1B	79.94(14)	N1D	Pt1D	N4D	104.20(13)
N2B	Pt1B	N4B	175.53(15)	N2D	Pt1D	N1D	79.77(13)
N3B	Pt1B	N1B	175.29(15)	N2D	Pt1D	N3D	96.06(13)
N3B	Pt1B	N2B	95.89(15)	N2D	Pt1D	N4D	175.94(13)
N3B	Pt1B	N4B	79.84(16)	N3D	Pt1D	N1D	174.79(12)
N4B	Pt1B	N1B	104.27(15)	N3D	Pt1D	N4D	80.03(13)
C1B	N1B	Pt1B	140.4(3)	C1D	N1D	Pt1D	139.2(3)
C1B	N1B	C4B	106.5(4)	C1D	N1D	C4D	107.2(3)
C4B	N1B	Pt1B	113.0(3)	C4D	N1D	Pt1D	113.3(3)
C5B	N2B	Pt1B	115.8(3)	C5D	N2D	Pt1D	115.7(3)
C5B	N2B	C6B	120.4(4)	C5D	N2D	C6D	121.8(3)
C6B	N2B	Pt1B	123.8(3)	C6D	N2D	Pt1D	122.3(2)
C8B	N3B	Pt1B	123.3(3)	C8D	N3D	Pt1D	123.7(2)
C9B	N3B	Pt1B	116.2(3)	C9D	N3D	Pt1D	115.4(3)
C9B	N3B	C8B	120.5(4)	C9D	N3D	C8D	120.9(3)
C10B	N4B	Pt1B	112.7(3)	C10D	N4D	Pt1D	113.0(3)
C13B	N4B	Pt1B	139.9(3)	C13D	N4D	Pt1D	140.1(3)

Atom	Atom	Atom	Angle/˚	Atom	Atom	Atom	Angle/˚
C13B	N4B	C10B	107.4(4)	C13D	N4D	C10D	106.8(3)
N1B	C1B	C2B	110.3(4)	N1D	C1D	C2D	110.9(4)
C3B	C2B	C1B	107.6(4)	C3D	C2D	C1D	105.8(4)
C2B	C3B	C4B	106.3(4)	C4D	C3D	C2D	107.3(4)
N1B	C4B	C3B	109.2(4)	N1D	C4D	C3D	108.8(4)
N1B	C4B	C5B	114.5(4)	N1D	C4D	C5D	114.8(4)
C3B	C4B	C5B	135.8(4)	C3D	C4D	C5D	136.2(4)
N2B	C5B	C4B	116.6(4)	N2D	C5D	C4D	116.3(4)
N2B	C6B	C7B	114.5(4)	N2D	C6D	C7D	114.4(3)
C8B	C7B	C6B	110.5(4)	C8D	C7D	C6D	110.6(3)
C14B	C7B	C6B	111.3(4)	C14D	C7D	C6D	110.6(3)
C14B	C7B	C8B	110.6(4)	C14D	C7D	C8D	111.3(3)
C14B	C7B	C15B	110.1(4)	C14D	C7D	C15D	110.9(3)
C15B	C7B	C6B	106.6(4)	C15D	C7D	C6D	106.0(3)
C15B	C7B	C8B	107.6(4)	C15D	C7D	C8D	107.2(3)
N3B	C8B	C7B	114.0(4)	N3D	C8D	C7D	114.9(3)
N3B	C9B	C10B	116.3(4)	N3D	C9D	C10D	117.1(4)
N4B	C10B	C9B	114.9(4)	N4D	C10D	C9D	114.5(4)
N4B	C10B	C11B	108.5(5)	C11D	C10D	N4D	109.1(4)
C11B	C10B	C9B	136.5(5)	C11D	C10D	C9D	136.4(4)
C12B	C11B	C10B	106.9(5)	C10D	C11D	C12D	107.5(4)
C11B	C12B	C13B	107.6(5)	C11D	C12D	C13D	106.6(4)
N4B	C13B	C12B	109.6(5)	N4D	C13D	C12D	110.1(4)

Table S4. Selected mean crystallographic and calculated structural and conformational parameters for compounds **1** and **2**.

	1		**2**	
	XRD	**DFT**	**XRD**	**DFT**
Bond distances (Å)				
Pt-$N_{pyrrole}$	2.011 (3)	2.026	2.013 (3)	2.026
Pt-N_{imine}	2.005 (3)	2.02	2.002 (3)	2.019
C=N	1.30 (5)	1.29	1.298 (5)	1.29
Bond angles (°)				
$N_{pyrrole}$-Pt-$N_{pyrrole}$	103.82 (14)	104.9	104.25 (14)	105.12
N_{imine}-Pt-N_{imine}	95.65 (14)	95.87	95.75 (14)	95.45
cis-$N_{pyrrole}$-Pt-N_{imine}	80.27 (14)	79.58	79.96 (13)	79.,66
trans-$N_{pyrrole}$-Pt-N_{immine}	175.50 (13)	175.04	175.27 (14)	174.54
C-$N_{pyrrole}$-C	107.05 (3)	107.48	106.91 (3)	107.5
C-N_{immine}-C	120.78 (3)	121.31	120.96 (4)	121.59

Table S5. Selected excited singlet states of TD-DFT calculations for complex **1** (CAM-B3LYP/DEF2-QZVP/GD3BJ in an acetonitrile solvent continuum).

Excited states	Energy/ eV	Wavelength (nm)	Oscillator strength		Major contributions (%)
1	3.4631	358	0.1163	Singlet-A	HOMO->LUMO (86%) H-3->LUMO (4%), H-2->L+1 (4%)
2	3.8112	324	0.2345	Singlet-A	H-1->LUMO (75%), HOMO->L+1 (19%)
3	3.9897	310	0.1042	Singlet-A	H-2->LUMO (53%), H-1->LUMO (12%), HOMO->L+1 (28%) H-3->L+1 (4%)
4	4.3064	287	0.0113	Singlet-A	H-4->LUMO (97%) H-3->LUMO (2%)
5	4.527	273	0.0005	Singlet-A	H-5->L+2 (12%), H-3->L+2 (13%), HOMO->L+2 (61%)
6	4.5794	270	0.3445	Singlet-A	H-3->LUMO (31%), H-1->L+1 (56%) H-2->L+1 (8%)
7	4.6797	264	0.0122	Singlet-A	H-4->L+2 (60%), H-2->LUMO (16%) H-3->L+1 (2%), H-1->LUMO (4%), HOMO->L+1 (7%)

Table S6. Selected excited singlet states of TD-DFT calculations for complex **2** (CAM-B3LYP/DEF2-QZVP/GD3BJ in an acetonitrile solvent continuum).

Excited states	Energy/ eV (λ nm)	Wavelength (nm)	Oscillator strength		Major contributions (%)
1	3.48	356	0.1249	Singlet-A	HOMO->LUMO (86%) H-3->LUMO (4%), H-2->L+1 (4%), H-1->L+1 (2%)
2	3.8327	323	0.2375	Singlet-A	H-1->LUMO (74%), HOMO->L+1 (20%)
3	4.0071	309	0.1061	Singlet-A	H-2->LUMO (54%), H-1->LUMO (13%), HOMO->L+1 (26%) H-3->L+1 (4%)
4	4.3339	286	0.0118	Singlet-A	H-4->LUMO (94%) H-3->LUMO (5%)
5	4.5513	272	0.0001	Singlet-A	H-5->L+2 (13%), H-3->L+2 (14%), HOMO->L+2 (64%)
6	4.5935	269	0.3738	Singlet-A	H-3->LUMO (31%), H-1->L+1 (56%) H-4->LUMO (2%), H-2->L+1 (8%)

Table S7. Summary of GLIDE XP docking scores and selected interaction energy parameters for HSA targets prepared from ligand-free and ligand-bound grids based on geometry-optimized (prepared) structures derived from PDB codes 1HA2 (HSA•{warfarin} complex), 2BXF (HSA•{diazepam} complex), and 2BXG (HSA•{ibuprofen}$_2$ complex). The docking runs were truncated to report only the top-scoring ligand pose for each ligand. All energies are in units of kcal mol^{-1}.

Ligand or drug	Binding site location	ligand effic.	ligand effic. sa	glide ligand effic. ln	XP GScore	glide Evdw	glide ECoul	glide energy	glide Einternal	glide Emodel	XP H Bond	XP Lipo. EvdW	XP EElectro
1HA2 - No warfarin bound in subdomain IIA of protein docking grid (Sudlow's Site I)													
ibuprofen	IA	-0.533	-1.315	-2.158	-8.001	-22.998	-1.285	-24.283	3.939	-31.178	0	-4.64	-0.096
Warfarin	IIA	-0.327	-0.929	-1.817	-7.513	-42.858	-2.647	-45.506	3.007	-63.649	-0.353	-5.865	-0.199
Diazepam	IIA-IIB	-0.251	-0.681	-1.256	-5.019	-25.042	-0.568	-25.610	1.048	-33.330	0	-3.979	-0.043
2	IA-IIA	-0.242	-0.657	-1.212	-4.843	-23.547	-0.339	-23.887	0.000	-30.228	0.000	-2.533	-0.025
1	IA-IIA	-0.243	-0.648	-1.171	-4.617	-23.762	-0.579	-24.341	0.325	-31.517	0.000	-2.614	-0.043
1HA2 - Warfarin bound in subdomain IIA of protein (Sudlow's Site I)													
Ibuprofen	IIIA	-0.590	-1.455	-2.387	-8.850	-26.042	-10.132	-36.174	8.038	-47.749	-0.667	-4.515	-0.760
Warfarin	IIIA	-0.365	-1.039	-2.032	-8.404	-35.237	-1.045	-36.282	5.918	-51.380	-0.541	-5.201	-0.078
Diazepam	IIIA	-0.295	-0.800	-1.476	-5.896	-32.921	0.055	-32.866	0.050	-43.701	-0.175	-4.435	0.004
2	IIA	-0.244	-0.662	-1.221	-4.880	-21.885	-3.481	-25.366	0.000	-28.067	-0.073	-2.544	-0.261
1	IIIA	-0.073	-0.195	-0.352	-1.390	-21.763	-2.510	-24.273	0.000	-34.975	-0.326	-2.596	-0.188
2BXF - No diazepam bound in subdomain IIIA of protein docking grid (Sudlow's Site II)													
Diazepam	IIIA	-0.452	-1.226	-2.260	-9.032	-44.241	-2.966	-47.207	1.236	-67.088	-0.688	-6.504	-0.222
Warfarin	IIIA	-0.318	-0.905	-1.770	-7.320	-33.986	-1.476	-35.462	4.800	-45.147	0	-6.367	-0.111
1	IIA-IIIA	-0.271	-0.723	-1.304	-5.145	-25.912	0.049	-25.863	0.325	-29.973	-0.697	-3.854	0.004
2	IIA-IIIA	-0.233	-0.633	-1.168	-4.666	-27.806	-0.203	-28.010	0.000	-35.104	0.000	-4.079	-0.015
Ibuprofen	IIIA	-0.287	-0.707	-1.159	-4.298	-20.072	-5.986	-26.058	1.780	-33.284	-1.111	-2.381	-0.449
2BXF - Diazepam bound in subdomain IIIA (Sudlow's Site II)													
Ibuprofen	IIA	-0.528	-1.302	-2.136	-7.922	-23.084	-5.223	-28.307	4.642	-39.436	-0.695	-2.911	-0.392
2	IIIA	-0.248	-0.674	-1.243	-4.967	-25.346	-0.204	-25.551	0.000	-33.215	0.000	-2.550	-0.015
1	IIIA	-0.106	-0.284	-0.513	-2.023	-22.867	-1.419	-24.286	0.324	-31.138	0.000	-1.879	-0.106
Warfarin	IB-IIIA cleft	-0.185	-0.526	-1.029	-4.257	-34.837	-2.655	-37.492	4.110	-49.074	-0.819	-3.158	-0.199
Diazepam	IIA-IIB	-0.190	-0.515	-0.949	-3.793	-34.404	-1.145	-35.549	0.175	-43.894	-0.123	-3.024	-0.086

2BXG - 2x ibuprofen bound, one in subdomain IIIA (Sudlow's Site II) and the second between subdomains IIA and IIB													
Ibuprofen	IIA-Trp214	-0.529	-1.304	-2.139	-7.932	-19.805	-3.976	-23.781	0	-27.136	0	-3.243	-0.298
2	IA-IIA	-0.240	-0.651	-1.200	-4.795	-22.218	0.478	-21.739	0.000	-30.041	0.000	-2.549	0.036
1	IA-IIA	-0.242	-0.645	-1.164	-4.593	-22.051	-0.508	-22.559	0.324	-29.124	0.000	-2.392	-0.038
Warfarin	IB-IIIA cleft	-0.197	-0.560	-1.094	-4.525	-31.451	-8.021	-39.472	4.671	-53.459	-1.341	-2.360	-0.602
Diazepam	IB-IIIA cleft	-0.180	-0.490	-0.903	-3.610	-28.813	-0.407	-29.220	0.369	-40.636	0	-3.212	-0.031

Table S8. Summary of Glide XP docking scores (as in Table S7) and selected interaction distances for HSA targets prepared from ligand-free grids based on geometry-optimized (prepared) structures derived from PDB codes 1HA2 (HSA•{warfarin} complex) and 2BXF (HSA•{diazepam} complex). The docking runs were truncated to report only the top-scoring ligand pose for each ligand. All energies are in units of kcal mol^{-1}.

Ligand or drug	Binding site location [a]	XP GScore	Distance to Trp-214 (Å) [b]	Closest tyrosine residues (Å) [b]	Closest phenylalanine residues (Å) [b]
1HA2 - No warfarin bound in subdomain IIA of protein docking grid (Sudlow's Site I)					
Ibuprofen	IA	-8.001	30.4	Tyr-30 (10.8), Tyr-150 (13.6), Tyr-148 (18.0)	Phe-19 (5.6), Phe-27 (7.5), Phe-49 (9.1)
Warfarin	IIA	-7.513	5.3	Tyr-150 (9.5), Tyr-263 (11.3), Tyr-452 (17.0)	Phe-211 (5.9), Phe-223 (8.3)
Diazepam	IIA-IIB	-5.019	11.3	Tyr-353 (11.9), Tyr-319 (12.2), Tyr334 (13.9)	Phe-206 (5.2), Phe-211 (11.3), Phe-330 (11.1)
1	IA-IIA	-4.843	11,6	Tyr-319 (12,4), Tyr-334 (16,7), Tyr-263 (16)	Phe-228 (7,7), Phe-326 (9), Phe-263 (10.1)
2	IA-IIA	-4.617	9,6	Tyr-319 (11.8), Tyr-332 (10,2), Tyr-334 (15)	Phe-228 (8,6), Phe-326 (9), Phe-211 (10,1)
2BXF - No diazepam bound in subdomain IIIA of protein docking grid (Sudlow's Site II)					
Diazepam	IIIA	-9.032	17.0	Tyr-411 (9.5), Tyr-452 (9.6), Tyr-341 (13.4)	Phe-403 (6.0), Phe-395 (9.0), Phe-488 (12.5)
Warfarin	IIIA	-7.320	17.0	Tyr-452 (9.5), Tyr-411 (10.4), Tyr-341 (13.3)	Phe-403 (5.3), Phe-395 (7.8), Phe-488 (12.2)
2	IIIA	-5.145	29.0	Tyr-370 (7.1), Tyr-353 (9,5), Tyr-319 (12.0)	Phe-403 (5.3), Phe-395 (7.8), Phe-488 (12.2)
1	IIIA	-4.666	30.0	Tyr-370 (5.9), Tyr-353 (9.6), Tyr-319 (11.3)	Phe-374 (13.7), Phe-309 (14.1), Phe-377 (14.4)
Ibuprofen	IIIA	-4.298	20.9	Tyr-411 (6.0), Tyr-452 (12.1), Tyr-341(19.3)	Phe-309 (12.1), Phe-374 (14.3), Phe-353 (14.0)

[a] Binding site regions (see **Footnote Figure** overleaf) are defined according to Figure 7 in the paper by Ghuman *et al*.[27] [b] Distance measured between the closest ring centroid pair of the ligand and residue. For metal chelates, the distance to the metal ion from the closest ring centroid is given.

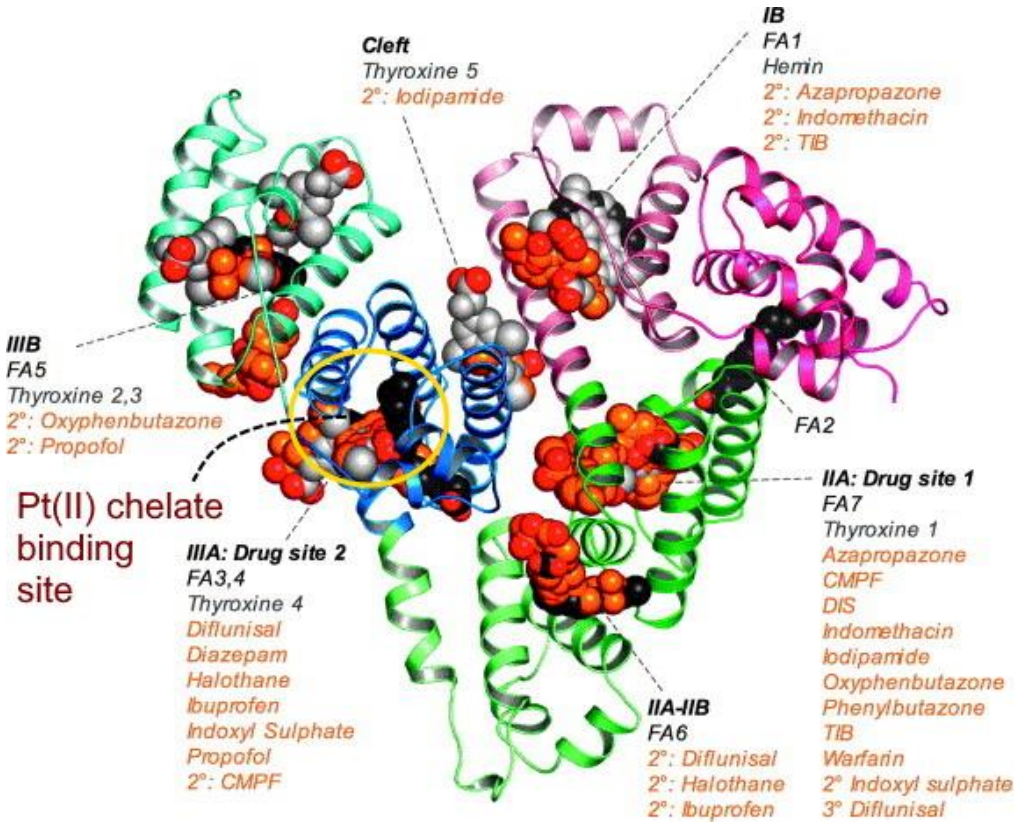

Footnote Figure: Modified from Figure 7 of Ghuman et al.[27]; "Summary of the ligand binding capacity of HSA as defined by crystallographic studies to date. Ligands are depicted in space-filling representation; oxygen atoms are coloured red; all other atoms in fatty acids (myristic acid), other endogenous ligands (hemin, thyroxin), and drugs are coloured dark grey, light grey, and orange, respectively." The yellow ellipse indicates where the most probable binding site is located for the Pt(II) chelates in the present docking and spectroscopic studies.

9. Extended TD-DFT electronic structure data for 1

Table S9. Full list of 60 TD-DFT-calculated excited singlet states (CAM-B3LYP/DEF2-QZVP/GD3BJ in a DMSO solvent continuum) for **1**. Six of the frontier MOs relevant for assignment of the transitions are shown in the first two rows; the last row of the table plots the calculated spectral envelope. State energies are uncorrected. DMSO was chosen as the solvent medium to allow assignment of both the NMR and UV-vis spectra of **1**.

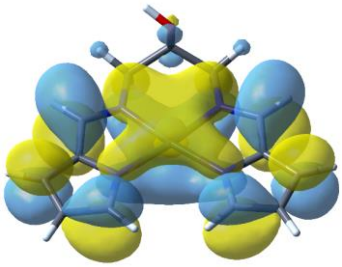

LUMO, L (–0.707 eV)

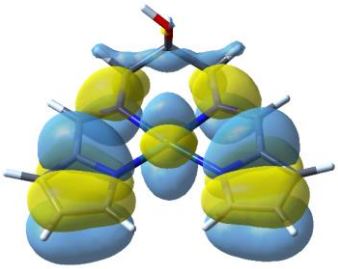

HOMO, H (–6.988 eV)

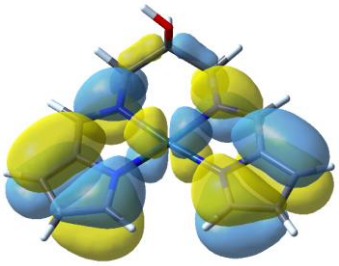

HOMO–1 (–7.095 eV)

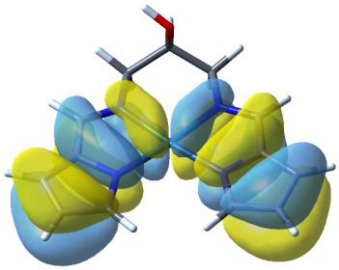

HOMO–2 (–7.618 eV)

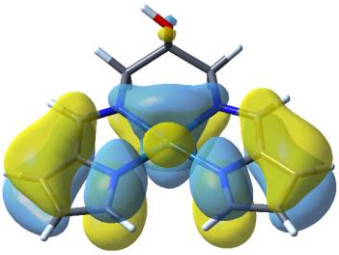

HOMO–3 (–8.042 eV)

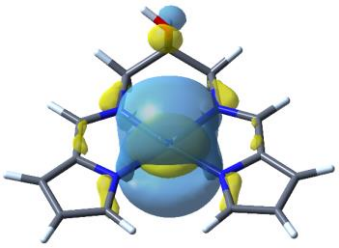

HOMO–4 (–8.154 eV)

Energy (cm^{-1})	Wavelength (nm)	Oscillator Strength	Major contribution	Top three minor contributions		
27,768.1	360.1	0.1316	HOMO→LUMO (86%)	H-3→LUMO (4%)	H-2→L+1 (4%)	H-1→L+1 (2%)
30,482.9	328.1	0.2577	H-1→LUMO (77%)	HOMO→L+1 (18%)		
32,012.1	312.4	0.1003	H-2→LUMO (54%)	H-1→LUMO (10%)	HOMO→L+1 (29%)	H-3→L+1 (4%)
34,906.9	286.5	0.0119	H-4→LUMO (97%)			
36,605.5	273.2	0.3798	H-3→LUMO (32%)	H-1→L+1 (57%)	H-2→L+1 (7%)	
36,934.5	270.7	0.0007	HOMO→L+4 (32%)	HOMO→L+6 (14%)	H-5→L+4 (6%)	H-5→L+6 (3%)
38,035.5	262.9	0.0543	H-4→L+4 (10%)	H-2→LUMO (33%)	HOMO→L+1 (27%)	H-5→L+1 (4%)
38,605.7	259.0	0.007	H-2→L+4 (13%)	H-1→L+4 (27%)	H-1→L+6 (11%)	H-7→L+4 (6%)
38,899.3	257.1	0.0308	H-4→L+4 (32%)	H-4→L+6 (16%)	HOMO→L+1 (14%)	H-4→L+1 (4%)
39,903.5	250.6	0.0007	H-4→L+1 (92%)			
40,505.2	246.9	0.1256	H-3→LUMO (53%)	H-2→L+1 (13%)	H-1→L+1 (20%)	H-7→L+1 (4%)
41,953.7	238.4	0.1572	H-5→LUMO (14%)	H-2→L+1 (57%)	H-1→L+1 (16%)	H-3→LUMO (3%)
43,474.1	230.0	0.0001	H-6→LUMO (80%)	H-5→LUMO (12%)		
44,019.3	227.2	0.0027	H-7→LUMO	H-3→L+1 (64%)	H-1→LUMO	H-1→L+3 (2%)

			(16%)		(2%)	
44,750.9	223.5	0.0005	H-6→L+3 (10%)	H-6→L+4 (37%)	H-6→L+6 (19%)	H-6→L+2 (6%)
46,401.9	215.5	0.0251	HOMO→L+2 (27%)	HOMO→L+3 (28%)	HOMO→L+5 (21%)	H-2→L+4 (3%)
47,046.3	212.6	0.0264	HOMO→L+3 (41%)	HOMO→L+5 (17%)	H-2→L+4 (5%)	H-1→L+2 (5%)
47,295.5	211.4	0.0036	H-1→L+2 (17%)	H-1→L+3 (13%)	H-1→L+5 (32%)	HOMO→L+6 (11%)
47,648.0	209.9	0.0081	H-7→L+1 (11%)	H-6→LUMO (12%)	H-5→LUMO (57%)	H-2→L+1 (9%)
48,027.9	208.2	0.0264	H-1→L+3 (49%)	H-1→L+4 (14%)	H-3→L+1 (3%)	H-2→L+3 (5%)
48,228.7	207.3	0.0026	H-2→L+4 (20%)	H-2→L+6 (14%)	H-1→L+4 (11%)	H-1→L+6 (11%)
48,480.4	206.3	0.001	H-7→LUMO (56%)	H-5→L+1 (20%)	H-6→L+1 (2%)	H-3→L+1 (8%)
49,000.6	204.1	0.0002	H-6→L+1 (73%)	H-5→L+1 (13%)		
50,045.1	199.8	0.0012	H-3→L+4 (21%)	H-3→L+6 (13%)	H-6→L+1 (7%)	H-5→L+4 (3%)
50,387.9	198.5	0.0029	H-2→L+5 (25%)	H-1→L+5 (11%)	HOMO→L+6 (28%)	H-3→L+4 (5%)
50,485.5	198.1	0.0234	HOMO→L+2 (26%)	HOMO→L+4 (15%)	HOMO→L+5 (27%)	H-2→L+5 (6%)
51,514.6	194.1	0.0043	H-3→L+5 (13%)	H-1→L+2 (13%)	H-1→L+6 (38%)	H-3→L+2 (5%)
51,558.2	194.0	0.008	H-1→L+2 (25%)	H-1→L+4 (16%)	H-1→L+5 (20%)	H-3→L+5 (3%)
52,395.4	190.9	0.0459	H-10→LUMO (16%)	H-9→LUMO (33%)	H-8→LUMO (15%)	H-4→L+3 (14%)
52,529.3	190.4	0.0002	H-2→L+3 (60%)	H-2→L+4 (11%)	H-2→L+2 (6%)	H-1→L+3 (5%)
52,911.6	189.0	0.0734	H-10→LUMO (28%)	H-8→LUMO (15%)	H-4→L+3 (28%)	H-9→LUMO (3%)
53,076.1	188.4	0.0481	H-9→LUMO (45%)	H-4→L+3 (23%)	H-10→LUMO (7%)	H-9→L+1 (3%)
54,298.1	184.2	0.0665	HOMO→L+10 (10%)	H-7→LUMO (5%)	H-5→L+1 (5%)	H-3→L+3 (4%)
54,339.2	184.0	0.0591	H-3→L+3 (13%)	HOMO→L+9 (13%)	H-7→L+1 (4%)	H-5→LUMO (2%)
54,633.6	183.0	0.0312	H-2→L+5 (15%)	H-8→LUMO (3%)	H-7→LUMO (7%)	H-5→L+1 (9%)
55,001.4	181.8	0.0116	H-2→L+6 (12%)	HOMO→L+7 (25%)	H-7→L+1 (4%)	H-4→L+2 (2%)
55,143.3	181.3	0.1163	H-10→LUMO (19%)	H-8→LUMO (45%)	H-8→L+1 (3%)	H-5→L+1 (2%)
55,286.9	180.9	0.0143	HOMO→L+7 (16%)	HOMO→L+10 (11%)	H-7→L+1 (9%)	H-4→L+5 (2%)
55,499.8	180.2	0.0271	H-2→L+6 (15%)	HOMO→L+7 (14%)	HOMO→L+8 (19%)	H-5→L+5 (4%)
55,601.4	179.9	0.0923	H-5→L+1 (36%)	H-8→LUMO (9%)	H-7→LUMO (5%)	H-6→L+1 (7%)
55,782.9	179.3	0.0234	H-7→L+1 (12%)	H-3→L+3 (28%)	H-4→L+2 (8%)	H-4→L+4 (2%)
56,207.2	177.9	0.0012	H-2→L+2 (35%)	H-2→L+4 (10%)	H-2→L+7 (5%)	H-2→L+8 (2%)
56,676.6	176.4	0.0002	H-1→L+8 (39%)	HOMO→L+13 (10%)	H-3→L+6 (8%)	H-2→L+2 (2%)
56,916.1	175.7	0.1546	H-2→L+10 (12%)	HOMO→L+16 (16%)	H-3→L+16 (4%)	H-2→L+9 (8%)
57,029.9	175.3	0.0552	H-1→L+7 (32%)	H-7→L+1 (2%)	H-3→L+4 (2%)	H-3→L+6 (7%)
57,044.4	175.3	0.0029	H-7→L+1 (39%)	H-4→L+2 (19%)	H-5→LUMO (4%)	H-4→L+4 (5%)
57,189.5	174.9	0.0201	H-3→L+5 (21%)	H-3→L+8 (3%)	H-2→L+4 (5%)	H-2→L+6 (7%)
57,369.4	174.3	0.0023	H-10→LUMO	H-10→L+1	H-9→L+1	H-8→L+1

			(10%)	(34%)	(18%)	(14%)
57,659.8	173.4	0.0019	H-10→L+1 (13%)	H-9→L+1 (48%)	H-20→LUMO (3%)	H-15→LUMO (5%)
57,983.2	172.5	0.0386	H-3→L+2 (13%)	H-1→L+16 (12%)	H-4→L+2 (4%)	H-3→L+4 (2%)
58,324.4	171.5	0.0029	H-3→L+5 (16%)	H-1→L+13 (12%)	H-7→L+4 (6%)	H-1→L+6 (8%)
58,439.7	171.1	0.0038	H-2→L+2 (13%)	H-5→L+3 (2%)	H-5→L+4 (8%)	H-3→L+4 (4%)
58,499.4	170.9	0.025		H-4→L+2 (7%)	H-4→L+5 (4%)	H-3→L+2 (5%)
58,747.8	170.2	0.0285	H-4→L+5 (28%)	H-8→L+2 (4%)	H-4→L+2 (7%)	H-3→L+4 (3%)
58,884.1	169.8	0.0237	H-4→L+5 (16%)	HOMO→L+9 (11%)	H-5→L+4 (2%)	H-4→L+2 (6%)
59,516.5	168.0	0.0136	H-7→L+4 (18%)	H-2→L+6 (15%)	H-7→L+2 (3%)	H-7→L+3 (5%)
59,824.6	167.2	0.0141	H-3→L+2 (25%)	H-10→L+1 (2%)	H-8→L+1 (6%)	H-8→L+2 (3%)
59,944.7	166.8	0.0537		H-4→L+6 (2%)	H-3→L+6 (4%)	H-2→L+7 (9%)
60,174.6	166.2	0.0176	H-8→L+1 (26%)	H-10→L+1 (8%)	H-8→L+2 (3%)	H-2→L+7 (5%)
60,227.8	166.0	0.0344	H-8→L+1 (19%)	H-10→L+1 (5%)	H-3→L+2 (3%)	H-3→L+6 (4%)

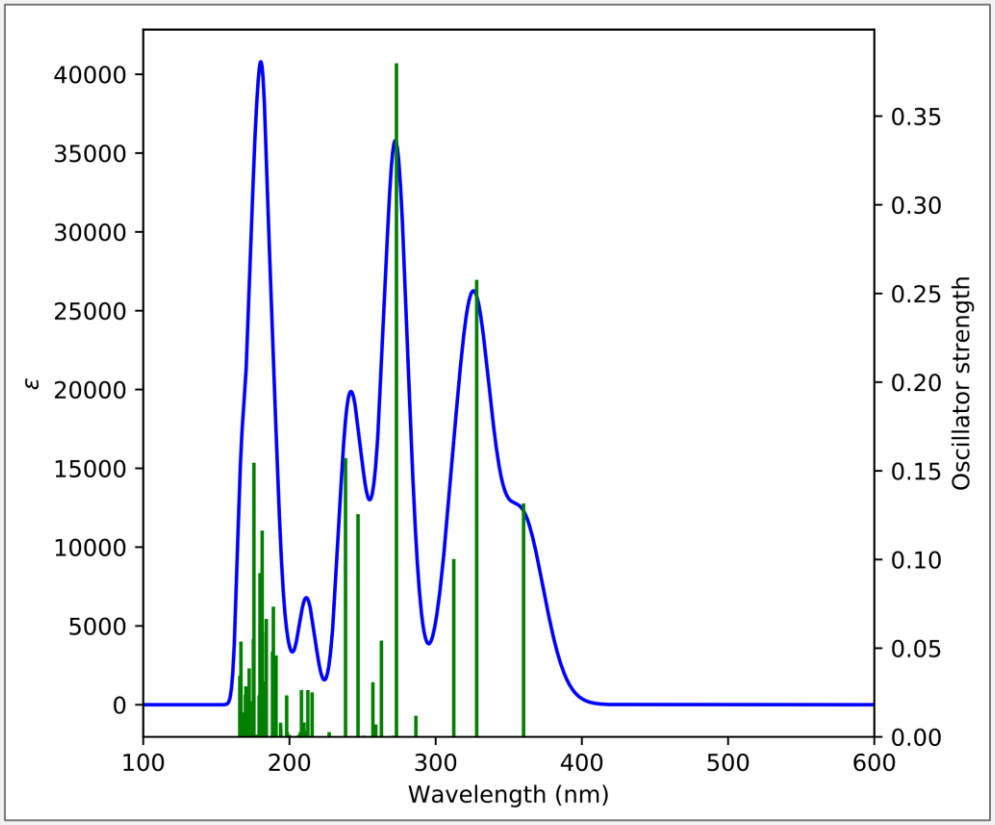

Table S10. Atomic (Cartesian) coordinates for the DFT-calculated structure of **1** (CAM-B3LYP/DEF2-QZVP/GD3BJ; DMSO solvent continuum).

atom	x	y	z
Pt	0.0007	0.0498	0.1403
O	0.0602	-3.0099	-1.5781
H	-0.6797	-3.4421	-2.0113
N	1.6098	1.2681	-0.017
N	1.4944	-1.3043	0.2343
N	-1.5028	-1.2939	0.2362
N	-1.6002	1.2797	-0.0148
C	-3.2601	2.7682	-0.234
H	-3.7641	3.7133	-0.3398
C	2.6843	-0.8234	0.1073
H	3.5494	-1.4765	0.1138
C	1.2739	-2.7217	0.4443
H	1.2223	-2.92	1.5159
H	2.1153	-3.2827	0.0402
C	-2.7963	0.5991	-0.0256
C	-0.0067	-3.2465	-0.1839
H	-0.0089	-4.3215	0.0147
C	-2.6895	-0.8039	0.111
H	-3.5595	-1.4504	0.1186
C	-3.846	1.5033	-0.1621
H	-4.8946	1.2625	-0.2005
C	3.2796	2.7451	-0.238
H	3.7902	3.6866	-0.3441
C	2.8011	0.5792	-0.0297
C	3.8568	1.4758	-0.1673
H	4.9036	1.2277	-0.2072
C	-1.2915	-2.7123	0.4427
H	-2.1391	-3.267	0.0391
H	-1.2468	-2.9178	1.514
C	-1.8789	2.5825	-0.1412
H	-1.1023	3.327	-0.1611
C	1.8975	2.5692	-0.1434
H	1.126	3.319	-0.1617

Table S11. Atomic (Cartesian) coordinates for the DFT-calculated structure of **1** (CAM-B3LYP/DEF2-QZVP/GD3BJ; water solvent continuum).

atom	x	y	z
Pt	0.0008	-0.0499	-0.14
O	0.0577	3.0095	1.5783
H	-0.6823	3.4423	2.0108
N	1.6108	-1.2676	0.0171
N	1.4939	1.305	-0.2342
N	-1.5032	1.2934	-0.2367
N	-1.6	-1.2804	0.0152
C	-3.2595	-2.7694	0.234
H	-3.7633	-3.7147	0.3395
C	2.6841	0.8249	-0.1075
H	3.5488	1.4783	-0.1144
C	1.2728	2.7224	-0.4441
H	1.2209	2.9206	-1.5157
H	2.114	3.2837	-0.0401
C	-2.7963	-0.6001	0.0257
C	-0.0083	3.2464	0.1838
H	-0.0108	4.3215	-0.0145
C	-2.6899	0.8031	-0.1114
H	-3.5599	1.4495	-0.1193
C	-3.8457	-1.5045	0.1619
H	-4.8944	-1.2637	0.1999
C	3.2814	-2.7438	0.2372
H	3.7926	-3.6851	0.3428
C	2.8016	-0.5779	0.0296
C	3.8578	-1.474	0.1665
H	4.9046	-1.2251	0.2059
C	-1.2924	2.7118	-0.4435
H	-2.1407	3.2662	-0.041
H	-1.2469	2.9169	-1.5149
C	-1.8784	-2.5835	0.1415
H	-1.1016	-3.3278	0.1613
C	1.8992	-2.5687	0.143
H	1.1282	-3.319	0.1614

10. References

1 O. V. Dolomanov, L. J. Bourhis, R. J. Gildea, J. A. K. Howard and H. Puschmann, *J. Appl. Crystallogr.*, 2009, **42**, 339–341.
2 G. M. Sheldrick, *Acta Crystallogr. Sect. Found. Adv.*, 2015, **71**, 3–8.
3 G. M. Sheldrick, *Acta Crystallogr. Sect. C Struct. Chem.*, 2015, **71**, 3–8.
4 X.-F. Shan, D.-H. Wang, C.-H. Tung and L.-Z. Wu, *Tetrahedron*, 2008, **64**, 5577–5582.
5 M. Van de Weert and L. Stella, *J. Mol. Struct.*, 2011, **998**, 144–150.
6 M. van de Weert, *J. Fluoresc.*, 2010, **20**, 625–629.
7 P. Geladi and B. R. Kowalski, *Anal. Chim. Acta*, 1986, **185**, 1–17.
8 J. G. Lees, A. J. Miles, R. W. Janes and B. A. Wallace, *BMC Bioinformatics*, 2006, **7**, 507.
9 J. T. Yang, C.-S. C. Wu and H. M. Martinez, in *Methods in Enzymology*, Academic Press, 1986, vol. 130, pp. 208–269.
10 T. Shiratori, S. Goto, T. Sakaguchi, T. Kasai, Y. Otsuka, K. Higashi, K. Makino, H. Takahashi and K. Komatsu, *Biochem. Biophys. Rep.*, 2021, **28**, 101153.
11 A. Micsonai, F. Wien, É. Bulyáki, J. Kun, É. Moussong, Y.-H. Lee, Y. Goto, M. Réfrégiers and J. Kardos, *Nucleic Acids Res.*, 2018, **46**, W315–W322.
12 S. Sookai and O. Munro, , DOI:10.26434/chemrxiv-2022-8v4x2.
13 M. J. Frisch, G. W. Trucks, H. B. Schlegel, G. E. Scuseria, M. A. Robb, J. R. Cheeseman, G. Scalmani, V. Barone, G. A. Petersson, H. Nakatsuji, X. Li, M. Caricato, A. V. Marenich, J. Bloino, B. G. Janesko, R. Gomperts, B. Mennucci, H. P. Hratchian, J. V. Ortiz, A. F. Izmaylov, J. L. Sonnenberg, D. Williams-Young, F. Ding, F. Lipparini, F. Egidi, J. Goings, B. Peng, A. Petrone, T. Henderson, D. Ranasinghe, V. G. Zakrzewski, J. Gao, N. Rega, G. Zheng, W. Liang, M. Hada, M. Ehara, K. Toyota, R. Fukuda, J. Hasegawa, M. Ishida, T. Nakajima, Y. Honda, O. Kitao, H. Nakai, T. Vreven, K. Throssell, J. A. Montgomery Jr., J. E. Peralta, F. Ogliaro, M. J. Bearpark, J. J. Heyd, E. N. Brothers, K. N. Kudin, V. N. Staroverov, T. A. Keith, R. Kobayashi, J. Normand, K. Raghavachari, A. P. Rendell, J. C. Burant, S. S. Iyengar, J. Tomasi, M. Cossi, J. M. Millam, M. Klene, C. Adamo, R. Cammi, J. W. Ochterski, R. L. Martin, K. Morokuma, O. Farkas, J. B. Foresman and D. J. Fox, *Gaussian 16 Revision C.01*, 2016.
14 T. Yanai, D. P. Tew and N. C. Handy, *Chem. Phys. Lett.*, 2004, **393**, 51–57.
15 F. Weigend and R. Ahlrichs, *Phys. Chem. Chem. Phys.*, 2005, **7**, 3297–3305.
16 S. Grimme, S. Ehrlich and L. Goerigk, *J. Comput. Chem.*, 2011, **32**, 1456–1465.
17 P. Fuentealba, H. Preuss, H. Stoll and L. Von Szentpály, *Chem. Phys. Lett.*, 1982, **89**, 418–422.
18 J. R. Cheeseman, G. W. Trucks, T. A. Keith and M. J. Frisch, *J. Chem. Phys.*, 1996, **104**, 5497–5509.
19 R. Ditchfield, *Mol. Phys.*, 1974, **27**, 789–807.
20 F. Lipparini, G. Scalmani, B. Mennucci, E. Cancès, M. Caricato and M. J. Frisch, *J. Chem. Phys.*, 2010, **133**, 014106.
21 R. Dennington, T. A. Keith and J. M. Millam, *GaussView Version 6*, 2019.
22 N. M. O'boyle, A. L. Tenderholt and K. M. Langner, *J. Comput. Chem.*, 2008, **29**, 839–845.
23 F. R. Clemente, T. Vreven and M. J. Frisch, in *Quantum Biochemistry*, John Wiley & Sons, Ltd, 2010, pp. 61–83.
24 A. K. Rappe, C. J. Casewit, K. S. Colwell, W. A. Goddard and W. M. Skiff, *J. Am. Chem. Soc.*, 1992, **114**, 10024–10035.
25 T. A. Halgren, R. B. Murphy, R. A. Friesner, H. S. Beard, L. L. Frye, W. T. Pollard and J. L. Banks, *J. Med. Chem.*, 2004, **47**, 1750–1759.
26 I. Petitpas, A. A. Bhattacharya, S. Twine, M. East and S. Curry, *J. Biol. Chem.*, 2001, **276**, 22804–22809.

27 J. Ghuman, P. A. Zunszain, I. Petitpas, A. A. Bhattacharya, M. Otagiri and S. Curry, *J. Mol. Biol.*, 2005, **353**, 38–52.
28 G. Madhavi Sastry, M. Adzhigirey, T. Day, R. Annabhimoju and W. Sherman, *J. Comput. Aided Mol. Des.*, 2013, **27**, 221–234.
29 F. Mohamadi, N. G. J. Richards, W. C. Guida, R. Liskamp, M. Lipton, C. Caufield, G. Chang, T. Hendrickson and W. C. Still, *J. Comput. Chem.*, 1990, **11**, 440–467.
30 W. L. Jorgensen and J. Tirado-Rives, *J. Am. Chem. Soc.*, 1988, **110**, 1657–1666.
31 G. A. Kaminski, R. A. Friesner, J. Tirado-Rives and W. L. Jorgensen, *J. Phys. Chem. B*, 2001, **105**, 6474–6487.
32 R. A. Friesner, J. L. Banks, R. B. Murphy, T. A. Halgren, J. J. Klicic, D. T. Mainz, M. P. Repasky, E. H. Knoll, M. Shelley, J. K. Perry, D. E. Shaw, P. Francis and P. S. Shenkin, *J. Med. Chem.*, 2004, **47**, 1739–1749.
33 J. R. Greenwood, D. Calkins, A. P. Sullivan and J. C. Shelley, *J. Comput. Aided Mol. Des.*, 2010, **24**, 591–604.
34 Z. Fakhar, B. Faramarzi, S. Pacifico and S. Faramarzi, *J. Biomol. Struct. Dyn.*, 2021, **39**, 6171–6183.